Charles University in Prague
Faculty of Mathematics and Physics

MASTER THESIS

František Gallovič

High frequency strong motion synthesis for k^{-2} rupture models

Supervisor: RNDr. Johana Brokešová, CSc.

Department of Geophysics
V Holešovičkách 2
180 00 Praha 8
Czech Republic

Prague 2002

Acknowledgements

I wish to express my sincere thanks to Johana Brokešová for her invaluable help and patience. Her helpful suggestions led to substantial improvement of the work. I am grateful to Jiří Zahradník for his advice and comments that contributed to expanding the scope of the thesis. I appreciate the invitation to IPGP by Pascal Bernard. He was kindly open to discussion. I would like to thank to the department staff and students for showing me the beauty of science. I am looking forward to more!

The deepest gratitude belongs to my parents for their support during my studies.

Many of the figures were made with Generic Mapping Tools (*Wessel and Smith*, 1991). The author was supported by the following grants: NATO Collaborative Linkage grant EST.CLG.976035, EU project EVG1-CT-1999-00001 PRESAP and several research projects in the Czech Republic - MSMT DG MSM/98-113200004, GACR 205/00/0902 and GAUK 176/2000/B GEO/MFF.

Prohlašuji, že jsem svou diplomovou práci napsal samostatně a výhradně s použitím citovaných pramenů. Souhlasím se zapůjčováním práce.

V Praze dne 19.4.2002 František Gallovič

Contents

Název práce: High frequency strong motion synthesis for k^{-2} rupture models
Autor: František Gallovič
Katedra: Katedra geofyziky
Vedoucí diplomové práce: RNDr. Johana Brokešová, CSc.
e-mail vedoucího: johana@seis.karlov.mff.cuni.cz
Abstrakt: Je diskutován výpočet stochastických silných pohybů půdy a jeho metodologické aspekty pro konečný zdroj. Trhlina je popsána stochastickým kinematickým modelem s k^{-2} rozložením skluzu (k je vlnové číslo). Zvláštní pozornost je věnována náběhovému času závislému na vlnovém čísle (*Bernard et al.*, 1996). V tomto modelu se trhlina šíří konstantní rychlostí jako puls o šířce L_0 (spojené s maximálním náběhovým časem). Nehomogenity skluzu menších charakterických rozměrů se vytvoří v čase úměrném jejich prostorové vlnové délce. Bylo zjištěno, že nejdůležitější část vlnového pole v 1D vrstevnatém modelu v lokálních vzdálenostech (< 50 km) je dána přímou S vlnou. V této práci se tedy uvažuje pouze tato. Používá se paprsková teorie. Paprsky jsou pro každý přijímač nalezeny z řídké sítě bodových zdrojů na zlomu. Nalezená paprsková řešení (časy šíření a komplexní amplitudy) jsou interpolovány do sítě dostatečně husté pro kinematické modelování. Heterogenní model skluzu je použit k modelování silných pohybů půdy během Aténského zemětřesení v roce 1999 ($M_w = 5.9$). Mapy maximálních hodnot zrychlení (PGA) počítáme pro různé k^{-2} modely skluzu s různými funkcemi rychlosti skluzu a pro několik hodnot L_0. Simulace jsou porovnány s publikovanými makroseismickými daty (intenzitami) a s výsledkem modelování nezávislou metodou.
Klíčová slova: kinematické modelování, k^{-2} skluz, silné pohyby půdy, PGA, Aténské zemětřesení.

Title: High frequency strong motion synthesis for k^{-2} rupture models
Author: František Gallovič
Department: Dept. of Geophysics
Supervisor: RNDr. Johana Brokešová, CSc.
Supervisor's e-mail address: johana@seis.karlov.mff.cuni.cz
Abstract: Stochastic strong motion synthesis with its methodological aspects for a finite fault is discussed. The rupture is described by a stochastic kinematic model with k^{-2} slip distribution (k being the wave number). Special attention is devoted to the wave-number dependent rise time (Bernard et al., 1996). In this model the rupture propagates with constant velocity in a slip pulse of width L_0 (connected with the maximum rise time). Slip inhomogeneities of shorter characteristic dimensions rupture in time proportional to their spatial wavelength. It was found that the most important contribution to the wave field in 1D medium consisting of homogeneous layers in near source range (< 50 km) is usually due to direct S waves and therefore only these waves are considered in this study. The ray theory is used. The rays for each receiver are traced from grid points distributed sparsely over the fault, and then the parameters of the ray solution (travel times and complex amplitudes) are interpolated by bicubic splines into a grid dense enough to perform kinematic modelling. The heterogeneous slip distributions is used to model the strong ground motions during the 1999 Athens earthquake ($M_w = 5.9$). The peak ground acceleration (PGA) maps have been computed for various k^{-2} slip models with various slip velocity functions and for several values of L_0. The simulations are compared with published observation data (macroseismic intensities), as well as with the previous modelling by an independent method.
Keywords: kinematic modelling, k^{-2} slip, strong motions, PGA, Athens earthquake.

Chapter 1

Introduction

Short fibres of cognition lead to a long thread of knowledge.

Strong ground motions are studied because they represent (besides surface ruptures) the most important seismic hazard during an earthquake. They can damage engineering structures and, consequently, injure or kill people who use them. To protect the structures, engineers need to know realistic ground motion estimation information about possible impact of a future earthquake. They are mainly interested in realistic broadband (about $0.5-20$ Hz) synthetic ground accelerations. One of the existing approaches to the task is the kinematic modelling of strong ground motion. This is the main topic of the presented work.

The strong motions are important also for seismologists because the recorded waveforms contain information about (among others) the dynamics of the rupture. The high frequency content of the ground acceleration is influenced by stopping and starting tends of sliding and short wavelength heterogeneities of the rupture process. These complexities are linked to complexities of the dynamic rupture properties studied by the fault mechanics, e.g., static and dynamic frictional coefficients, strength, etc. Unfortunately, the information about the source is masked by propagation effects, which make this problem difficult and not yet resolved.

High frequency numerical modelling of finite extent sources requires strong computing power (large computer memory and high processor speeds). Fortunately, great improvement in computers as well as in computer science allows for such calculations nearly in real time.

In this chapter we briefly describe the motivations for this work. Next we introduce the physical quantities and derive basic formulas, which are used in the text. We give a brief discussion on source scaling laws in the section 1.3. The rupture models used by seismologists in strong motion prediction are discussed in chapter 2 with emphasis on kinematic models. The "k^{-2}" broadband rupture model is discussed in detail and generalized. The strong motion synthesis together

with the asymptotic Green's function computation is discussed in the chapter 3. In the chapter 4, the theory and methodical aspects discussed in the previous chapters are applied to modelling of strong ground motion for the 1999 Athens earthquake.

1.1 Motivation

There are two main motivations for this work. The first one is to find a way to model past earthquakes to determine some characterization of the rupture process. This is done for the 1999 Athens earthquake in Chap. 4. The second one is the task of strong ground motion prediction for an unknown (future) earthquake.

To address the latter a EU project PRESAP has to be mentioned. PRESAP is an acronym for "Towards Practical, Real-time Estimation of Spatial Aftershock Probabilities: a Feasibility Study in Earthquake Hazard". Its aim is to find out whether the following procedure of prediction of strong aftershock and its impact could give reasonable results and whether it could be done in nearly real-time: After a strong earthquake, its fault plane solution is determined. The slip inversion is then performed. The resulting slip model is used to compute the redistribution of the static stress in the vicinity of the earthquake on oriented planes. The stress map is compared with the map of active geological faults and if there is found a correlation, it is characterized as an area where a strong aftershock can occur. The possible magnitude is estimated. The ground shaking (our task) is then computed in the near source region. After the local conditions (site effects) are taken into account, the possible dangers in urban areas can be estimated.

The project is based on indications given by seismologists in case of, e.g., Landers earthquake ($M = 7.3$), see *King et al.*, 1994. The static stress redistribution is well correlated with the small aftershocks as well as with the Big Bear earthquake ($M = 6.4$), which occurred about 3 hours after the main shock. A large aftershock can also occur much later.

Note that in some cases the strong aftershocks can be more devastating than the main shock. The current thrilling example is a series of two strong earthquakes in the Hindu Kush region, Afghanistan. On March 3, 2002 a $M = 7.4$ event occurred 256 km beneath the surface. It caused death of at least 113 people; most of them were killed due to landslide triggered by the quake. This shock was followed by a shallow earthquake (hypocentral depth of 8 km) on March 25 with $M = 6.1$. This quake caused more causalities (at least 1,500 people killed) and damage than the previous one of intermediate depth. Could have been this second earthquake triggered by the previous one? Are the seismologists able to predict such strong aftershock? These questions are very important and not yet resolved. The aim of this study is to try to answer a more specific question whether we can predict realistic ground motions caused by an earthquake of a

given size and location.

1.2 Basic equations

The seismic source and its radiation is well investigated problem in elastodynamics. The displacement $\boldsymbol{u}$ measured at $\boldsymbol{r}$ caused by the seismic moment tensor distribution $\mathbf{M}$ corresponding to a seismic fault Σ is given by the representation theorem (see, e.g., *Aki and Richards*, 1980)

$$u_i(\boldsymbol{r},t) = \iint\limits_{\Sigma} d\boldsymbol{\xi} G_{ij,k}(\boldsymbol{r},t;\boldsymbol{\xi}) * M_{jk}(\boldsymbol{\xi},t), \tag{1.1}$$

where $\mathbf{G}$ is the elastodynamic Green's tensor, $\boldsymbol{\xi}(x,z)$ represents the position on the fault, $*$ means the time convolution and comma in the subscript denotes the spatial derivative. The seismic moment tensor for shear slip on the fault is given by:

$$M_{jk}(\boldsymbol{\xi},t) = \mu(\boldsymbol{\xi})\Delta u(\boldsymbol{\xi},t)\left[n_j(\boldsymbol{\xi})\nu_k(\boldsymbol{\xi}) + n_k(\boldsymbol{\xi})\nu_j(\boldsymbol{\xi})\right], \tag{1.2}$$

where μ is the rigidity, Δu the slip function (discontinuity of displacement), $\boldsymbol{\nu}$ and $\boldsymbol{n}$ are the unit normal to the fault and the unit vector in the slip direction, respectively.

Farra et al., 1986, introduced the impulse response of a medium to a point double couple dislocation source:

$$H_i(\boldsymbol{r},t;\boldsymbol{\xi}) = \mu(\boldsymbol{\xi})n_j(\boldsymbol{\xi})\nu_k(\boldsymbol{\xi})\left[G_{ij,k}(\boldsymbol{r},t;\boldsymbol{\xi}) + G_{ik,j}(\boldsymbol{r},t;\boldsymbol{\xi})\right]. \tag{1.3}$$

Using (1.2) and (1.3) we can express (1.1) as

$$\boldsymbol{u}(\boldsymbol{r},t) = \iint\limits_{\Sigma} d\boldsymbol{\xi}\boldsymbol{H}(\boldsymbol{r},t;\boldsymbol{\xi}) * \Delta u(\boldsymbol{\xi},t). \tag{1.4}$$

For simple media, the calculation of $\boldsymbol{H}$ can be done analytically or using some approximations. For more complicated media, $\boldsymbol{H}$ can be determined numerically by, for example, the finite differences, the discrete wave-number method or asymptotic methods (e.g., the ray theory).

Spudich and Frazer, 1984, proposed that in smooth models it is often possible to represent $\boldsymbol{H}$ only by the "far-field" part of the complete Green's function (ray approximation for given elementary wave):

$$\boldsymbol{H}(\boldsymbol{r},t;\boldsymbol{\xi}) = \boldsymbol{H}_0(\boldsymbol{r};\boldsymbol{\xi})\dot{\Delta}(t - T(\boldsymbol{r};\boldsymbol{\xi})), \tag{1.5}$$

where $\boldsymbol{H}_0$ is the ray amplitude, $\Delta(t) = \delta(t) - i/(\pi t)$ is the analytic function of Dirac's delta function δ, the dot above Δ means the time derivative and T denotes the travel time. The equation (1.5) is a general formula for all types of

rays (reflected, transmitted, converted etc.). The calculation of $\boldsymbol{H}_0$ using the ray theory is discussed in detail in section 3.1.

It should be noted that $\boldsymbol{H}_0$ is generally complex vector. The resultant synthetic seismogram can be obtained by taking the real part of the representation theorem.

The ray approximation can be applied only with some restrictions, otherwise the computed wave-field won't be valid. The main constraint is that all wavelengths under consideration should be much shorter than the distance to the fault and the widths of layers. The validity and accuracy of the far-field approximation of the Green's function is discussed in, e.g., *Červený et al.*, 1977, *Červený*, 1985, *Farra et al.*, 1986, etc.

We put (1.5) into (1.4) and after expressing the convolution, we can write the representation theorem in simple form

$$\boldsymbol{u}(\boldsymbol{r},t) = \iint\limits_{\Sigma} d\boldsymbol{\xi}\boldsymbol{H}_0(\boldsymbol{r};\boldsymbol{\xi})\Delta\dot{u}(\boldsymbol{\xi},t-T(\boldsymbol{r};\boldsymbol{\xi})), \tag{1.6}$$

where $\Delta\dot{u}$ is the analytic function of the time derivative of the slip function.

For homogenous unbounded medium, the travel time can be expressed as $d(\boldsymbol{r};\boldsymbol{\xi})/c$, where d is the distance between the source and the receiver. $\boldsymbol{H}_0$ is given by

$$\boldsymbol{H}_0(\boldsymbol{r};\boldsymbol{\xi}) = \frac{\mu\boldsymbol{F}^c(\boldsymbol{r};\boldsymbol{\xi})}{4\pi\rho c^3 d(\boldsymbol{r};\boldsymbol{\xi})}, \tag{1.7}$$

where ρ is the density, c either P or S wave velocity, $\boldsymbol{F}^c$ is the radiation pattern depending on the takeoff angles of the ray at the source and the geometrical properties of the fault (strike, dip, rake).

We put (1.7) into equation (1.6) and obtain the representation theorem for homogeneous space:

$$\boldsymbol{u}(\boldsymbol{r},t) = \frac{\mu}{4\pi\rho c^3}\iint\limits_{\Sigma} d\boldsymbol{\xi}\frac{\boldsymbol{F}^c(\boldsymbol{r};\boldsymbol{\xi})}{d(\boldsymbol{r};\boldsymbol{\xi})}\Delta\dot{u}\left(\boldsymbol{\xi},t-\frac{d(\boldsymbol{r};\boldsymbol{\xi})}{c}\right). \tag{1.8}$$

Let us introduce the point source approximation of the source. We assume that the variations of d and $\boldsymbol{F}^c$ when changing $\boldsymbol{\xi}$ are negligible with respect to the hypocentral distance d_0 (e.g., corresponding to the nucleation point of the rupture). Equation (1.8) then gives

$$\boldsymbol{u}(\boldsymbol{r},t) = \frac{\mu\boldsymbol{F}^c(\boldsymbol{r})}{4\pi\rho c^3 d_0}\Omega\left(t-\frac{d_0}{c}\right), \quad \Omega(t) = \iint\limits_{\Sigma} d\boldsymbol{\xi}\Delta\dot{u}(\boldsymbol{\xi},t), \tag{1.9}$$

where $\Omega(t)$ is called the *source time function*. The point source approximation is suitable for small earthquakes.

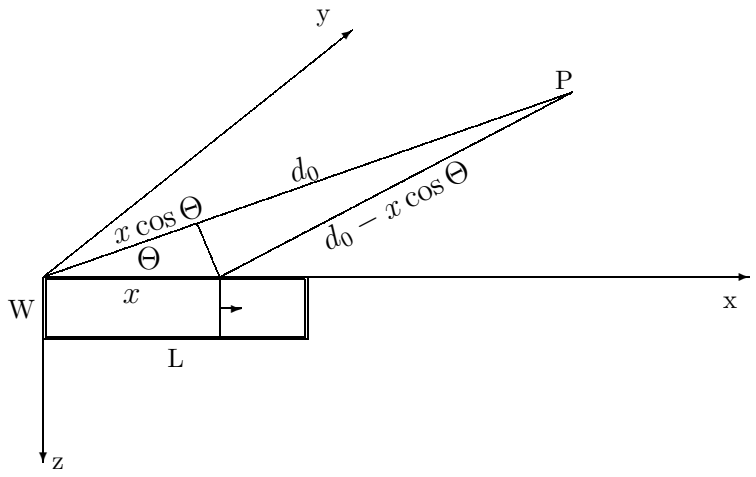

Figure 1.1: The geometry used for a line fault with unilateral rupture propagation. The coordinate system is connected with the fault. The rupture propagates in the x direction. The approximation of the distance from a point on the fault to a receiver P by $d \doteq d_0 - x\cos\Theta$ is called the Fraunhoffer's approximation.

Another, weaker, approximation of the source is called the "partial" finite source approximation. We return back to (1.8) and assume that the variations of $\boldsymbol{F}^c$ when changing $\boldsymbol{\xi}$ are negligible with respect to the hypocentral distance d_0. We make the same assumption for d outside the argument of $\Delta\dot{u}$ only. We obtain

$$\boldsymbol{u}(\boldsymbol{r},t) = \frac{\mu \boldsymbol{F}^c(\boldsymbol{r})}{4\pi\rho c^3 d_0}\Omega(\boldsymbol{r},t), \quad \Omega(\boldsymbol{r},t) = \iint\limits_{\Sigma} d\boldsymbol{\xi}\Delta\dot{u}\left(\boldsymbol{\xi}, t - \frac{d(\boldsymbol{r};\boldsymbol{\xi})}{c}\right), \tag{1.10}$$

where $\Omega(\boldsymbol{r},t)$ is called the *apparent source time function* due to its dependence on the position of the receiver.

Let us express $\Delta\dot{u}(\boldsymbol{\xi},t) = D(\boldsymbol{\xi})U(\boldsymbol{\xi},t)$ where $D(\boldsymbol{\xi})$ represents the final slip and $U(\boldsymbol{\xi},t)$ is a function normalized to unite final dislocation.

Let us assume that the points along the fault follow similar slip history, but at different times, as the rupture front expands. We will refer this slip rate history as the slip velocity function and the time necessary for the rupture front to reach point $\boldsymbol{\xi}$ on the fault the rupture time $t_r(\boldsymbol{\xi})$. We write

$$\Delta\dot{u}(\boldsymbol{\xi},t) = D(\boldsymbol{\xi})U(\boldsymbol{\xi}, t - t_r(\boldsymbol{\xi})). \tag{1.11}$$

In this case, U is already the slip velocity function. The duration of U is called the rise time.

Let us assume a very simple model of nearly line rupture with unilateral propagation. We consider the coordinate system corresponding to the fault as

shown in Fig. 1.1. The final slip $D(x,z)$ is constant along z and the slip velocity function is the same for each point. The rupture is assumed to propagate at constant rupture velocity v, thus, we can express the dependence of the rupture time on the spatial coordinate x as $t_r(x) = x/v$. We assume the Fraunhoffer's approximation, which suggests that the distance d can be approximated by the relation $d = d_0 - x\cos\Theta$, where Θ is the angle between the direction of rupture propagation and the seismic ray connecting the source with the receiver. Under all above mentioned assumptions the equation (1.10) is simplified to

$$\boldsymbol{u}(\Theta,t) = \frac{\mu W \boldsymbol{F}^c}{4\pi\rho c^3 d_0} \int_0^L D(x) U\left(t - \frac{d_0}{c} + \frac{x}{c}\cos\Theta - \frac{x}{v}\right) dx, \tag{1.12}$$

where W is the width of the fault (see Fig. 1.1). The Fraunhoffer's approximation is valid only for observers situated far from the fault with respect to the length of the fault.

Note that in this approximation the integration with respect to z is an integration along an isoline of sum of the rupture time and the propagation time. Such isoline is called the isochrone and can have more general shape for general 2D rupture in complex media.

We omit expressing the dependence on Θ further in the text. We introduce the well known directivity coefficient:

$$C_d = \frac{1}{1 - (v/c)\cos\Theta}. \tag{1.13}$$

Using (1.13) we can rewrite (1.12) into the form

$$\boldsymbol{u}\left(t + \frac{d_0}{c}\right) = \frac{\mu W \boldsymbol{F}^c}{4\pi\rho c^3 d_0} \int_0^L dx D(x) U\left(t - \frac{x}{vC_d}\right). \tag{1.14}$$

Transforming (1.14) to the Fourier domain and considering magnitude of $\boldsymbol{u}$ ($u = |\boldsymbol{u}|$) only we obtain

$$u(f) = C \int_0^L dx D(x) U(f) e^{-i2\pi f \frac{x}{vC_d}} \quad \text{with} \tag{1.15}$$

$$C = \frac{\mu W F^c}{4\pi\rho c^3 d_0} e^{-i2\pi f d_0/c}.$$

1.3 Source scaling laws and source time function

In the seismological literature various source scaling laws (empirical relations between earthquake and rupture properties) can be found. These laws are very

Rupture Area [km^2] vs. Seismic Moment	$A = 2.23 \times 10^{-15} \times M_0^{2/3}$
Average slip [cm] vs. Seismic Moment	$\Delta\bar{u} = 1.56 \times 10^{-7} \times M_0^{1/3}$
Average slip duration [sec] vs. Seismic Moment	$T_R = 2.03 \times 10^{-9} \times M_0^{1/3}$
Area of Fault Covered by Asperities	22%
Average Asperity Slip Contrast	2.01

Table 1.1: Scaling Relations of Slip Models after *Somerville et al.*, 1999. Seismic moment is in dyne-cm.

important when we want to predict strong ground motions of a future earthquake. We can either choose all the parameters (for usually the worst scenario possible in the region) or choose only a few of them and determine the remaining ones by using some scaling law relation.

The selection of parameters to be chosen depends on the technique of ground motion modelling. Let us name some of the most important properties which have to be known for modelling: the scalar seismic moment M_0, the length L and the width W of the fault, the static stress-drop $\Delta\sigma$, the mean slip $\Delta\bar{u}$, etc. There are other useful properties such as the area of the largest asperity, hypocentral distance to the closest asperity, hypocentral distance to the largest asperity or slip duration. The empirical scaling laws for all of these properties can be found in seismological literature. The rupture slip distributions and its properties are discussed in Appendix A.

The main problem of the scaling relations is that they are derived from generally small group of earthquakes and from quantities determined quite inaccurately. It results in a big variance of any studied quantity.

Mai and Beroza, 2000, divided the earthquakes into two groups – strike-slip and dip-slip events. These two groups differ in scaling laws mainly between the seismic moment and dimensions of the rupture area. Here we write only some of the basic laws given by *Mai and Beroza*, 2000 (L and W are in km, $\Delta\bar{u}$ is in cm and M_0 in Nm):

Strike-slip events:

$$\begin{aligned} \log L &= 0.36 \log M_0 - 5.15 \\ \log W &= 0.09 \log M_0 - 0.54 \\ \log \Delta\bar{u} &= 0.55 \log M_0 - 8.68 \end{aligned}$$

Dip-slip events:

$$\begin{aligned} \log L &= 0.38 \log M_0 - 5.71 \\ \log W &= 0.33 \log M_0 - 4.93 \\ \log \Delta\bar{u} &= 0.29 \log M_0 - 3.88 \end{aligned} \tag{1.16}$$

Some of the scaling laws presented by *Somerville et al.*, 1999, are in the table 1.1.

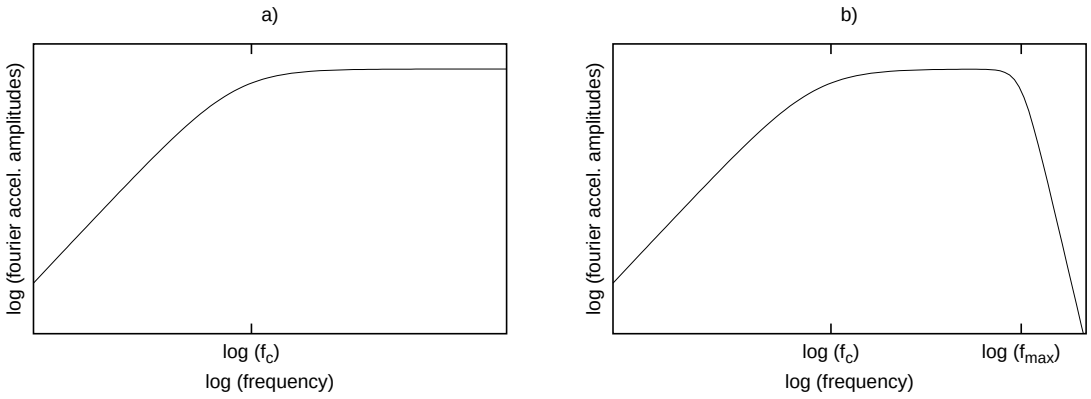

Figure 1.2: Model source spectrum $\ddot{\Omega}(f)$ (accelerogram) with a) one corner frequency f_c due to the finiteness of the rupture process, influenced by the directivity and b) with two corner frequencies: f_c and the so-called f_{max}. Note the f^2 slope before f_c, the plateau between the corner frequencies and the steep fall-off after f_{max}. The height of the plateau of $\ddot{\Omega}(f)$ is proportional to $f_c^2 M_0$.

The fault mechanics as well as the empirical observations show that the mean slip is proportional to $\Delta\sigma L$. Assuming constant stress drop (i.e., the same for earthquakes of various sizes), the mean slip is proportional to the fault length. Such scaling law is usually referred in the seismological literature as the constant stress drop scaling.

Among the most important scaling laws belong the one for the source time function. Empirically, it was found that the (apparent) source time functions obtained from far-field as well as near-field recordings exhibit f^{-2} decay of amplitudes in the Fourier domain beyond a corner frequency f_c which corresponds to the reciprocal of the total duration of the rupture process. This property of $\Omega(f)$ is referred in the seismological literature as ω-squared model of the source time function. The shape of such source spectrum can be represented by

$$\Omega(f) \propto \frac{M_0}{1 + (f/f_c)^2}. \tag{1.17}$$

When a short period or broadband seismograph is used, a rapid decay of amplitudes can be found after a frequency called f_{max}. Examples of two accelerogram source spectra (with and without f_{max}) are in the figure 1.2.

The presence of f_{max} is very important. If it is present it causes a steep spectral fall-off at high frequencies of the accelerogram and subsequently weaker damages caused by the earthquake. There are two main hypothesis to explain the existence of f_{max}. Some authors think it is connected with the attenuation of high frequency waves due to propagation in dissipative medium, others that it is a source controlled parameter. For example, f_{max} is modelled by the slip function in kinematic model of *Hisada*, 2000. For more details about f_{max} see *Hanks*, 1992.

Chapter 2

Kinematic models of earthquake ruptures

There are various approaches to the representation of the rupture processes on an extended fault in order to simulate the strong ground motions. The approaches can be divided into four overlapping groups:

Kinematic. In this approach we are not interested in dynamics of the rupture. We want to find only the main (realistic) kinematic properties of the fault which would generate desired ω-squared spectrum as it is described in section 1.3. The kinematic model defines the slip distribution and the rupture time as functions of position on the fault. Radiated wave-field is then simply calculated by the integral in the representation theorem. Numerically, the integral can be transformed into the sum over the point sources with their own Green's functions and slip histories.

The synthesis is valid in arbitrary distances from the fault. The only problem is to compute Green's functions.

Composite. The fault is divided into relatively few segments which are assumed to represent small earthquakes. The source time function of each subevent has its spectral shape, corner frequency, seismic moment, etc. Contributions of subevents are summed in a special way to get proper seismic moment and spectral shape of the source function corresponding to the whole fault. This approach is often used together with the Empirical Green's Function (EGF) method where an aftershock is taken as the record of the small rupture, but analytic Green's function can be used as well. More about composite modelling can be found in papers by, e.g. *Frankel*, 1991, *Irikura and Kamae*, 1994, and others.

Stochastic. We are interested in the high frequency processes on the fault only in a stochastic sense. The aim is just to describe deterministically an envelope (low frequencies) of the seismogram to correspond to given seismic moment, corner frequency, duration, etc., for the whole earthquake. The high frequencies are purely stochastic. See *Beresnev and Atkinson*, 1997.

These models are usually used just for fast prediction. The main problem is that this modelling approach has nearly no physics in the background.

Hybrid. For different frequency bands the seismogram is modelled by either kinematic (composite) or stochastic approach. The threshold frequency is usually about 1Hz (lower frequencies are deterministic, higher stochastic). See *Zahradník and Tselentis* (submitted) and others.

In this study, we consider only the kinematic modelling. Quite a lot of models of rupture propagation and its scaling properties were proposed to obtain desired ω-squared source time function. They differ mainly in definition of the kinematic quantities used for calculation of the wave-field. Input kinematic quantities are usually as follows:

- spatial distribution of final slip values
- temporal slip function at each point on the fault
- rise time (time needed for creation of the slip at a given point)
- rupture time (time needed by the rupture front to reach a given point)

Some of the kinematic models are referred to by *Hisada*, 2000, or *Hartzell at al.*, 1999, e.g.:

- Haskell source model
- Omega-square model
- "k^{-2}" kinematic source model

In this text, the classic Haskell model is presented only briefly because it is well known. In this work we discuss in detail the k^{-2} kinematic model only. The source time functions are derived and discussed for a very simple rupture model (line fault, unilateral propagation etc.) in a homogenous space. Our simplified properties of the rupture can be understood as an approximation for the observer situated far from the fault. Then we *extrapolate* the model to more general rupture (rectangular fault, radial rupture propagation).

2.1 Haskell source model

The description of Haskell model of a line fault can be found in many textbooks on seismology. The fault of length L is characterized by unilateral rupture propagation with constant velocity v, uniform final slip D and boxcar slip velocity function with the duration (rise time) τ, same for any point on the fault. Under these assumptions, it is easy to obtain the amplitude spectrum from (1.15):

$$|u(f)| = \frac{W\mu F^c}{4\pi\rho c^3 d_0} D \frac{sin(\tau\pi f)}{\tau\pi f} \frac{sin\left(\frac{L\pi f}{vC_d}\right)}{\frac{L\pi f}{vC_d}}. \tag{2.1}$$

For meaning of the quantities in (2.1) see section 1.2.

Formula (2.1) yields two corner frequencies, one connected with the rise time and the other with the apparent duration of the rupture propagation. Although (2.1) satisfies ω-squared spectral law behind the larger of the two frequencies and exhibits observed directivity effect, it is not sufficient. Problems are obvious when looking into the acceleration in time domain. The displacement is a convolution of two boxcars which yields a trapezoid function. Then, the acceleration consists only of four peaks, which is not realistic. It can be masked by convolution with a long-duration Green's function.

The real broad-band accelerograms are complicated even more, both in time and spectral domain. These complications are caused by a lot of factors, e.g. more complicated final slip on the fault and/or non-constant rupture velocity. The rupture process is completely inhomogeneous, not perfectly planar and contains asperities with large slip release. All these effects together with complexity of propagation of seismic waves cause observed complicated high frequency radiation.

The other problem of Haskell model is the extrapolation of this model to more general rupture (rectangular fault, etc.). Since the isochrones are parallel to z-axis of the fault (see fig. 1.1), it radiates ω-squared spectrum. However, *Bernard and Herrero*, 1994 showed that because the isochrones have more general direction for observer near the fault, it generates rather f^3 spectral decay. Such problem is one of the most important because the observations exhibit also in the near field ω-squared spectral shape.

We need to find more realistic finite source model. One of the most novel is discussed in the next section. We use the Haskell model in section 3 in cases when we are interested more in seismic waves propagation than in the rupture model.

2.2 "k^{-2}" kinematic source model

In this chapter, we introduce the main assumptions and free kinematic parameters of the set of so-called k^{-2} rupture models. We show that they generate the source time functions which satisfy the ω-squared scaling law. In order to analytically derive the influence of the kinematic parameters on the generated wave field, we study them for a line fault in the Fraunhoffer's approximation in homogeneous medium. In Sec. 2.2.4, we extrapolate the model to a rectangular fault and show how to compute the wave fields in general media.

We adapt the equation (1.15) for our purposes. Since the slip distribution $D(x)$ is identically zero outside the fault (i.e., for $x < 0$ and $x > L$), the limits of the integral in the formula (1.15) can be extended to infinity. We can write

$$u(f) = C' \int_{-\infty}^{\infty} dx D(x) U(f) e^{-i\frac{2\pi f x}{vC_d}} \quad \text{with} \tag{2.2}$$

$$C' = \frac{\mu W F^c}{4\pi\rho c^3 d_0} e^{-i2\pi f d_0/c}.$$

Further, we omit writing the limits of the integral. Note that (2.2) depends on the angle from the fault due to the directivity coefficient C_d.

2.2.1 Instantaneous slip

We start with simple k^{-2} rupture model with instantaneous slip. Under instantaneous slip we understand that the final slip at each point on the fault is finished instantaneously. Mathematically, we assume that the slip velocity function $U(t) = \delta(t)$. We put the Fourier transform of $U(t)$ ($U(f) = 1$) into the equation (2.2) obtaining

$$u(f) = C' \int dx D(x) e^{-i\frac{2\pi f x}{vC_d}}. \tag{2.3}$$

We express the final slip $D(x)$ using the inverse Fourier transform of the wave number spectrum $D(k_x)$. We get

$$u(f) = C' \int dx \int dk_x D(k_x) e^{i2\pi k_x x} e^{-i\frac{2\pi f x}{vC_d}}. \tag{2.4}$$

Integrating it with respect to x,

$$u(f) = C' \int dk_x D(k_x) \delta\left(k_x - \frac{f}{vC_d}\right) \tag{2.5}$$

and then with respect to k_x, we obtain

$$u(f) = C' D(k'_x), \quad k'_x = \frac{f}{vC_d}. \tag{2.6}$$

As we can see from the formula (2.6), the Fourier frequency spectrum of displacement $u(f)$ at a given frequency corresponds to the Fourier wave number spectrum of the slip distribution $D(k_x)$ at the wave number $k'_x = \frac{f}{vC_d}$. Consequently, the spectral decay of the apparent source time function corresponds to the spectral decay of the dislocation distribution. *Bernard and Herrero*, 1994, introduced the so-called k^{-2} slip distribution $D(k_x)$ in the form (amplitude spectrum) $|D(k_x)| = \Delta\bar{u}L$ for $k_x < 1/L$ and $|D(k_x)| = \Delta\bar{u}L/(k_x L)^2$ for $k_x > 1/L$,

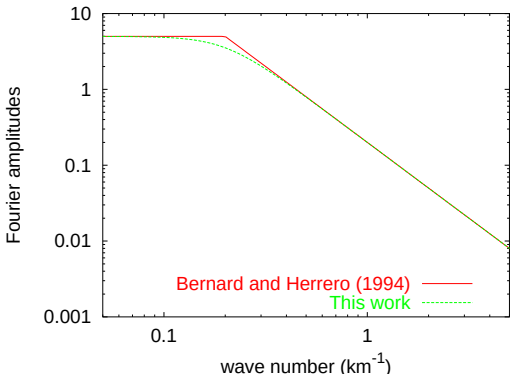

Figure 2.1: The slip distribution spectra: the difference between Bernard's and Herrero's definition of the k^{-2} slip model and the definition (2.7) in this work. The only difference is in the vicinity of the corner wave number where our definition behaves smoothly.

where L is the length of the fault, $\Delta\bar{u}$ represents the average slip and $k_x = 1/L$ is called the corner wave number.

In this work, we use modified smoothed dislocation distribution with generalized corner wave number $k_x^c = K/L$ as follows:

$$D(k_x) = \frac{\Delta\bar{u}L}{\sqrt{1 + \left(\frac{k_x L}{K}\right)^4}} e^{i\Phi(k_x)}, \tag{2.7}$$

where Φ is the phase spectrum. As we can see from figure 2.1, the amplitude spectra of the above mentioned slip distributions differ in intermediate wavenumbers only. They are not so important for us since we are interested in the spectral k^{-2} decay at high frequencies.

Let us note that since we assume the constant stress drop scaling ($\Delta\bar{u} \sim L$), (2.7) represents a self-similar distribution. It means that if the length of the fault is changed, only the long wavelengths of slip feel the change, unlike the short ones (for $k_x \to \infty$, $|D(k_x)| = K^2/k_x^2$ is independent of L). In other words, the dimension of the rupture affects only large wavelengths. The Fourier spectral amplitudes of small wavelengths are the same for any size of the fault (see fig. 2.2).

Note that, generally, we do not make any restriction to the phase spectrum of $D(k_x)$. So, it can be, e.g., chosen randomly.

Let us put the equation (2.7) into (2.6). Considering the amplitude spectrum only, we get

$$|u(f)| = |C'| \frac{\Delta\bar{u}L}{\sqrt{1 + \left(\frac{fL}{vC_dK}\right)^4}}. \tag{2.8}$$

Expressing C' (see Eq. (2.2)) and considering the definition of the scalar seismic

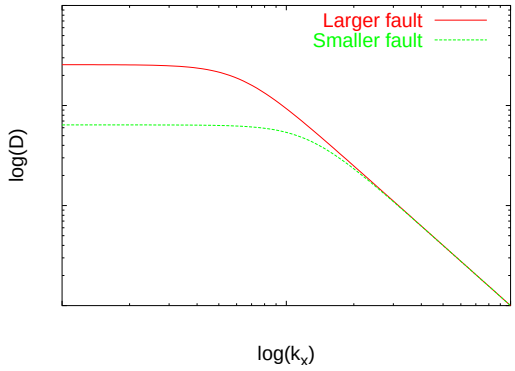

Figure 2.2: The amplitude spectra of the k^{-2} slip distribution for two different sizes of the fault. The figure shows that for wave numbers less then the corner frequency of the smaller fault the Fourier spectrum is affected by the dimension of fault, but for higher wave numbers it is not.

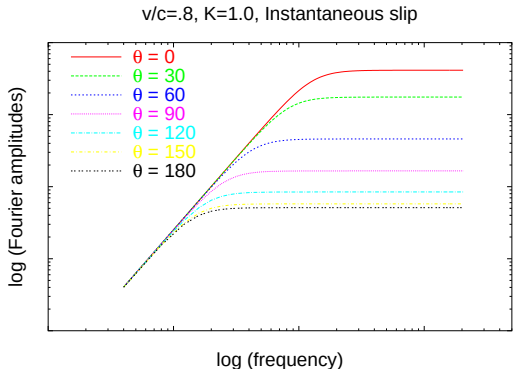

Figure 2.3: The apparent acceleration source time function spectra generated by the k^{-2} rupture model with instantaneous slip for various values of Θ. Note the angular dependence of the apparent corner frequency and the spectral plateau.

moment $M_0 = \mu \Delta \bar{u} L W$ the equation (2.8) gives

$$|u(f)| = \frac{F^c}{4\pi\rho c^3 d_0} \frac{M_0}{\sqrt{1 + \left(\frac{fL}{vC_d K}\right)^4}}. \tag{2.9}$$

As we can see from Eq. (2.9), our above mentioned assumptions give a rupture model which satisfies the ω^2 scaling law (see Sec. 1.3). The apparent acceleration source time function spectra computed according to the formula (2.9) for various angles Θ from the fault (see Fig. 1.1) can be found in the figure 2.3. Note that our smooth character of the slip distribution results in smooth acceleration spectrum.

The apparent corner frequency can be expressed as

$$f_a = \frac{vC_d K}{L} \tag{2.10}$$

and we can see that it varies with different angles from the fault due to C_d (see the formula (1.13)). The typical values of C_d for a reasonable choice $v/c = 0.8$ can be found in the figure 2.4.

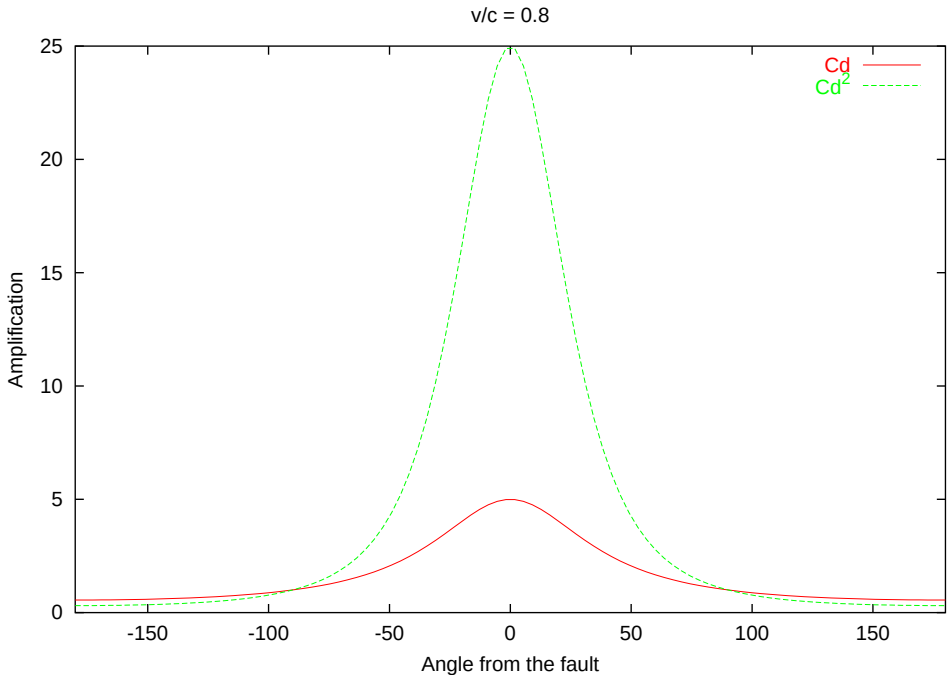

Figure 2.4: Graph showing the dependence of C_d and C_d^2 on the angle from the fault (according to Eq. (1.13)). The former one is connected with the apparent source time function, the latter one with the acceleration spectral level.

The height of the spectral plateau of the apparent source time function can be found as the limit of (2.9) multiplied by $4\pi^2 f^2$ for infinite frequency:

$$|\ddot{u}(f \to \infty)| = \frac{\pi F^c M_0}{\rho c^3 d_0} f_a^2. \tag{2.11}$$

As we can see from Eq. (2.11), the height of the spectral plateau is proportional to C_d^2 due to the proportionality to the square of the apparent corner frequency. The graph of angular dependence of C_d^2 can be found in Fig. 2.4. It represents a very strong directivity effect. For $v/c = 0.9$, C_d^2 would reach 100 in the direction of rupture propagation. Such high frequency amplification is not realistic. Consequently, the rupture model needs a revision concerning the high frequency range.

Note that, regardless of the position of the station, the K-parameter (coming from the corner wave number of the dislocation distribution) influences the corner frequency similarly as C_d does and, consequently, it affects the height of the acceleration spectral plateau. Moreover, K does not influence the seismic moment. That is why we can link it to the high frequency features of the k^{-2} rupture model.

2.2.2 Wave number dependent boxcar slip function

Bernard et al., 1996, proposed a revised kinematic model to damp the strong amplification at high frequencies due to directivity. The authors preserve the k^{-2} slip distribution and define a more realistic slip velocity function, boxcar with the wave number dependent rise time $\tau(k_x)$:

$$U(k_x;t) = H[t+\tau(k_x)]H[\tau(k_x)-t]\frac{1}{\tau(k_x)}, \tag{2.12}$$

where H is the Heaviside function.

The idea of the wave number dependent rise time arises from dynamic models of earthquake ruptures or cracks where the dislocation on small scales is created earlier than the dislocation on large scales. This phenomenon was also found in inversions of rupture propagation (i.e. *Wald and Heaton*, 1994, *Cotton and Campillo*, 1995).

The wave-number dependent rise time should be understood in the following sense: after arrival of the rupture front to a point on the fault, the creation of slip at all wave-numbers k_x starts. The dislocation at given k_x reaches the final value $D(k_x)$ at the time $\tau(k_x)$. Consequently, the slipping at the point is finished after τ_{max} =max($\tau(k_x)$). Note that we assume that the rupture time does not depend on the wave number.

To involve the above discussed feature in Eq. (2.2), we can assume that (2.2) was derived for a rupture process at given wave number. For a given wave number, the generated wave field is given by

$$u(k_x;f) = C' \int dx D(k_x;x) U(k_x;f) e^{-i\frac{2\pi f x}{vC_d}}, \tag{2.13}$$

where $D(k_x;x)$ represents the final slip distribution for given wave number k_x, i.e., $D(k_x;x) = D(k_x)e^{i2\pi k_x x}$. To obtain the whole wave field generated by the rupture process at all wave numbers, we integrate (2.13) with respect to k_x. It results in

$$u(f) = C' \int dk_x \int dx D(k_x) e^{i2\pi k_x x} U(k_x;f) e^{-i\frac{2\pi f x}{vC_d}}. \tag{2.14}$$

Considering the time Fourier transform of $U(k_x;t)$ given by Eq. (2.12) and rearranging the terms in (2.14) we obtain

$$u(f) = C' \int dk_x \int dx D(k_x) \frac{\sin(\pi f \tau(k_x))}{\pi f \tau(k_x)} e^{\pi f \tau(k_x)} e^{i2\pi x\left(k_x - \frac{f}{vC_d}\right)}. \tag{2.15}$$

We apply the same trick as in case of instantaneous slip. We integrate with respect to x which yields

$$u(f) = C' \int dk_x D(k_x) \frac{\sin(\pi f \tau(k_x))}{\pi f \tau(k_x)} e^{\pi f \tau(k_x)} \delta\left(k_x - \frac{f}{vC_d}\right) \tag{2.16}$$

and then with respect to k_x to get the final formula

$$u(f) = C' D(k'_x) \frac{\sin(\pi f \tau(k'_x))}{\pi f \tau(k'_x)} e^{\pi f \tau(k'_x)}, \quad k'_x = \frac{f}{v C_d}. \tag{2.17}$$

We have to propose a relation between the rise time and the wave number. Two parameters were introduced by *Bernard et al.*, 1996, in order to quantify the relation. 1) τ_{max} which controls maximum duration of slip and 2) a nondimensional coefficient a which controls, for given wavelength λ, the ratio of the rise time to the time necessary for the rupture front to pass the distance λ. The authors suggested $a = 0.5$, which is used in this text. The maximum rise time τ_{max} is controlled by the width of the so-called propagation pulse L_0 according to the relation $\tau_{max} = L_0/v$. The observational evidences for such pulse propagating over the fault are given by *Heaton*, 1990.

Bernard et al., 1996, introduced the relation between the rise time $\tau(k_x)$ and the wave number in the following form: $\tau(k_x) = \tau_{max}$ for $k_x < a/L_0$ and $\tau(k_x) = a\tau_{max}/(L_0 k_x)$ for $k_x > a/L_0$. In other words, for scales equal or larger then L_0, the slipping is finished in time τ_{max}, for smaller scales the rise time is proposed to be proportional to the reciprocal of the wave number.

In this work we use a smoothed rise time distribution:

$$\tau(k_x) = \frac{\tau_{max}}{\sqrt{1 + \left(\frac{L_0 k_x}{a}\right)^2}}, \quad \tau_{max} = \frac{L_0}{v}. \tag{2.18}$$

The difference between the above mentioned relations for the rise time concerns the intermediate wave-numbers only (similarly to the case of the smooth slip distribution, see Fig. 2.1). Our smooth character of the relation results in smooth acceleration spectrum.

Note that the equation (2.18) represents a k^{-1} self-similar distribution of $\tau(k_x)$. It means that the large wavelengths are affected by the width of the slip pulse while the small wavelengths are not (see Fig. 2.5).

To illustrate the difference between the propagation of the rupture with constant and wave number dependent rise time, we show the spatio-temporal evolution of such rupture models in the figure 2.6. Although the rupture propagation seems to be quite similar, the radiated wave field would be different a lot. Constant boxcar slip function would excite f^{-3} spectral decay at high frequencies of the seismogram because it would act as a low-pass filter.

Since the computation of rupture evolution of the model with constant rise time is obvious, let us discuss the computational approach for the model with the wave number dependent rise time. The dislocation at given wave number $D(k_x; x)$ is filtered (i.e., multiplied) by the slip history $S(k_x; x, t_r)$ on the fault corresponding to the given rupture time t_r and k_x. Summing the contributions from all wave numbers we obtain the state of the slip on the fault at the time t_r

$$d(x, t_r) = \int D(k_x) e^{i2\pi k_x x} S(k_x; x, t_r) dk_x. \tag{2.19}$$

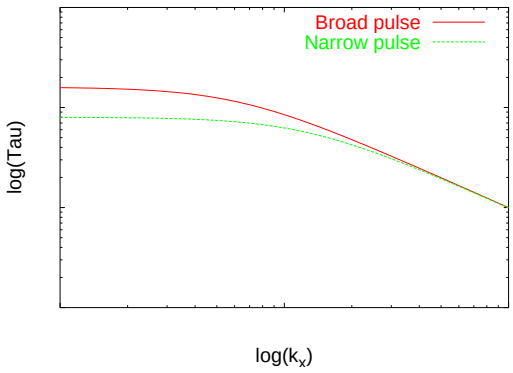

Figure 2.5: The k^{-1} rise time distribution $\tau(k_x)$ for two different sizes of propagating slip pulse: The picture shows the same self-similar spectral effect as in the figure 2.2 but for the widths of the slip pulses.

Note that (2.19) is not a simple inverse Fourier transform since S depends on x. It should be noted that S could represent the slip velocity history on the fault. Then, $d(x, t_r)$ would give the spatial-temporal evolution of the slip velocities on the fault.

Acceleration amplitude spectra given by (2.17) multiplied by $4\pi^2 f^2$ together with (2.18) and (2.7) are presented in the figure 2.7 for two widths of the propagation pulse. As it can be seen, the spectra should be studied in three frequency ranges separated by two corner frequencies (unlike the model with instantaneous slip which spectral shape consists of two ranges split by one corner frequency only). They are illustrated in Fig. 2.8. The first corner frequency is the apparent corner frequency f_a (2.10) controlled by the dislocation distribution (2.7). The second one, called the *transition frequency*

$$f_0 = aC_d \frac{v}{L_0} = a\frac{C_d}{\tau_{max}}, \tag{2.20}$$

is connected with the corner wave number of the rise time distribution (2.18). It is influenced by the directivity coefficient and the duration of the propagating slip pulse τ_{max}. Note that $f_a < f_0$ since $K/L < a/L_0$.

At low frequencies ($f < f_a$), $u(f)$ is not affected by the finite duration of the boxcar. It means that the C_d^2 proportional amplification (see the model with instantaneous rise time) is preserved. Between f_a and f_0 (middle frequencies), the boxcar slip velocity function of finite duration starts to act as a low-pass filter. However, behind the transition frequency (high frequencies), the k^{-1} proportionality of the rise time forces the source acceleration spectrum to be independent on frequency (see the behaviour of the argument of the sinc function in Eq. (2.17)), i.e., we obtain a plateau at high frequencies. Thus, this model is consistent with the ω-squared scaling law.

The height of the plateau can be examined by the value of the acceleration

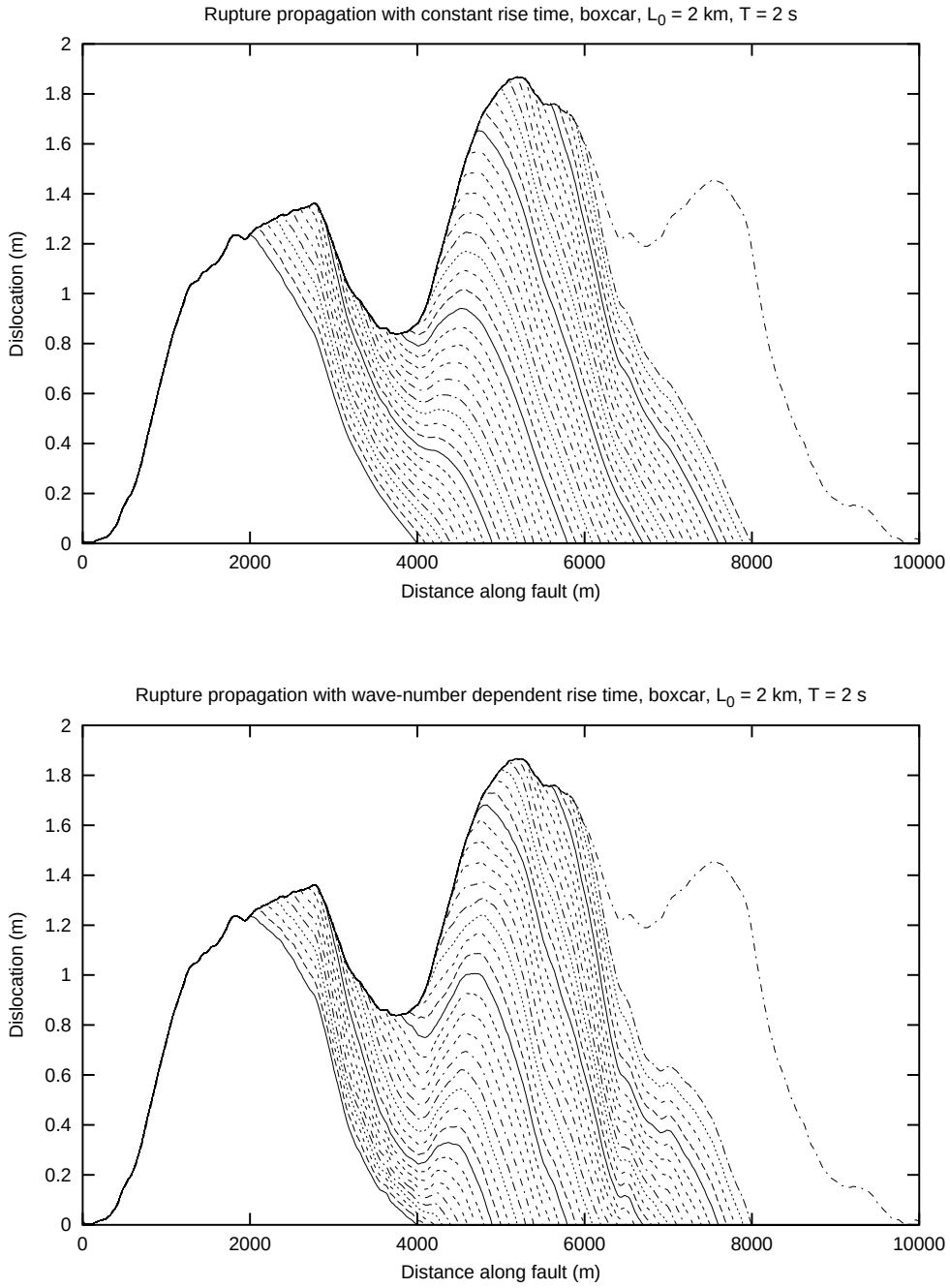

Figure 2.6: Spatial-temporal evolution of two rupture models with the boxcar slip function. In the top figure the rise time is constant, in the bottom it is wave-number dependent according to the relation (2.18). Each curve represents the state of the rupture in equally spaced time steps. Note that in the wavenumber dependent case the dislocations of smaller wave-lengths are finished earlier than the dislocations of larger wavelengths.

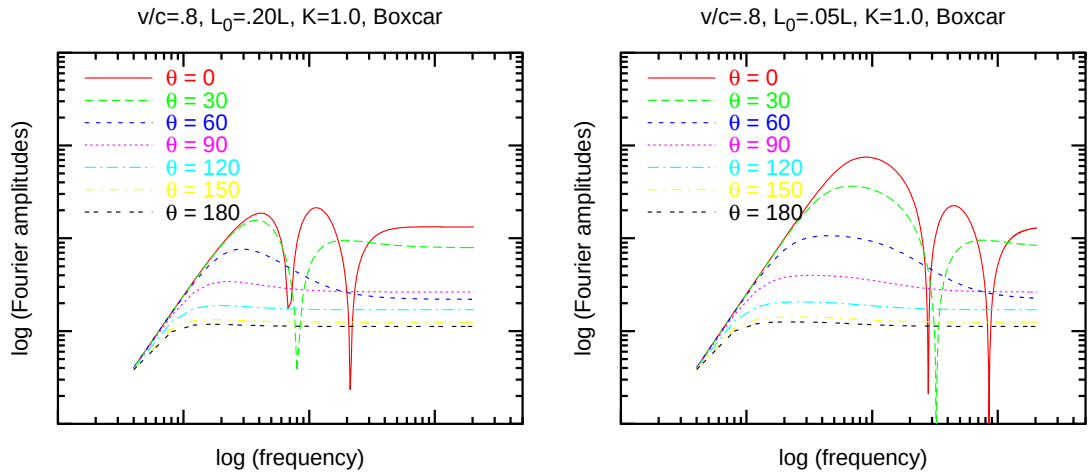

Figure 2.7: Amplitude spectra of acceleration generated by the k^{-2} rupture model with the boxcar slip velocity function for two widths of the propagating pulse ($L_0 = 0.20L$ and $L_0 = 0.05L$). Note that the amplification at high frequencies is weaker than in the case of the instantaneous slip (see Fig. 2.3). The ranges of axis are the same as in the figure 2.3.

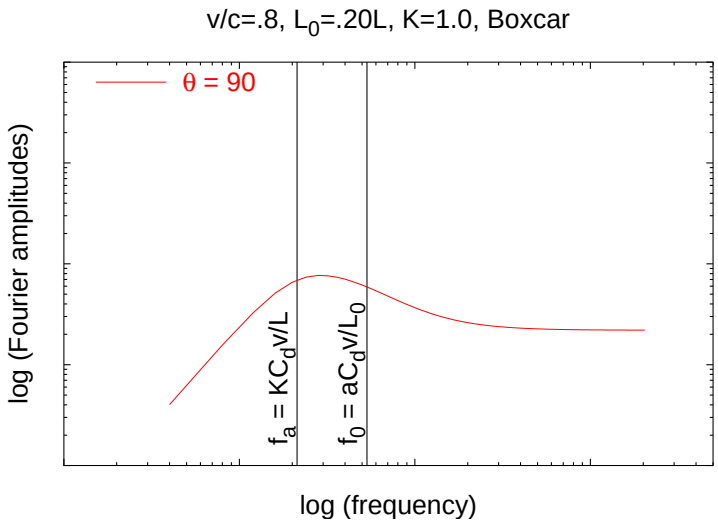

Figure 2.8: The figure shows the acceleration spectra and the two corner frequencies of the rupture model with wave number dependent rise time for a special choice of parameters (listed above the figure). The ranges are the same as in Fig. 2.3.

source spectra for infinite frequency:

$$|\ddot{u}(f \to \infty)| = \frac{\pi F^c M_0}{\rho c^3 d_0} f_a^2 \frac{sin(\pi a C_d)}{\pi a C_d}. \tag{2.21}$$

We can see that the directivity dependence of the acceleration plateau is decreased (comparing with the result for the instantaneous slip) by a factor of $\mathrm{sinc}(\pi a C_d)$. This results in more realistic estimates of seismograms in the direction of rupture propagation.

It should be noted that as the transition frequency approaches the apparent corner frequency (by increasing L_0), the frequency range with strong C_d^2 amplification contracts. Observational evidence to prefer $L_0 = .20L$ over $L_0 = 0.05L$ is missing.

2.2.3 General slip function

The boxcar slip velocity function remains unrealistic. Here we show how it can be replaced by a general function.

We take a function $F(t)$ with one-second duration and unit finite dislocation. The slip velocity function for given rise time $\tau(k_x)$ is then $U(k_x; t) = F(t/\tau(k_x))/\tau(k_x)$. The unit dislocation is preserved due to the factor $1/\tau(k_x)$. Fourier transform of $U(k_x; t)$ is $U(k_x; f) = X(f\tau(k_x))$, where $X(f)$ is the Fourier spectrum of $F(t)$. We put it into the equation (2.14):

$$u(f) = C' \int dk_x \int dx D(k_x) e^{i2\pi k_x x} X(f\tau(k_x)) e^{-i\frac{2\pi f x}{vC_d}}. \tag{2.22}$$

We integrate with respect to x and then with respect to k_x (like in previous sections) to obtain

$$u(f) = C' D(k'_x) X(f\tau(k'_x)), \quad k'_x = \frac{f}{vC_d}. \tag{2.23}$$

As in the previous section, the source spectrum (2.23) can be studied in three frequency ranges. The described effects are similar. Again, the plateau at high frequencies is a consequence of the k^{-2} slip distribution and the k^{-1} dependence of the rise time, regardless of the slip velocity function. We can obtain the height of the plateau by limiting the frequency to infinity in (2.23) multiplied by $4\pi^2 f^2$ as follows:

$$|\ddot{u}(f \to \infty)| = \frac{\pi F^c M_0}{\rho c^3 d_0} f_a^2 X(aC_d). \tag{2.24}$$

Let us introduce two slip velocity functions that are used in this text. The first one is the Brune's function

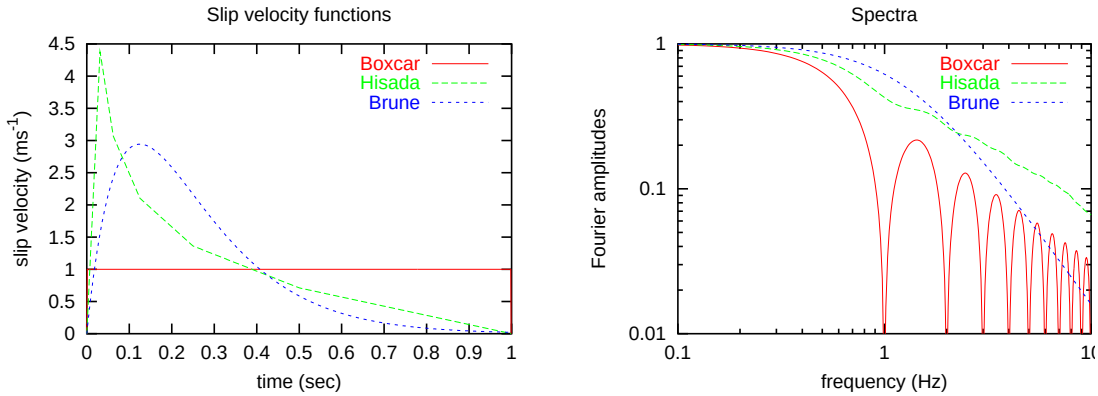

Figure 2.9: Three slip velocity functions with their spectra used in this study. The Hisada's function is constructed according to *Hisada*, 2000 for a special choice of parameters describing the function: $N_V = 5$ and $f_{max} = 16s^{-1}$. The Brune's function is computed according to (2.25) with $f_b = 8s^{-1}$. Note that the functions satisfy the definition conditions for $F(t)$, namely the one second duration and the unit finite dislocation.

$$F(t) = \begin{cases} f_b^2 t e^{-f_b t}, & t \geq 0 \\ 0, & t < 0 \end{cases} \tag{2.25}$$

and the second one is the Hisada's function constructed according to a procedure described by *Hisada*, 2000. Both of them together with the boxcar function (for comparison) and their amplitude spectra are displayed in the figure 2.9.

Acceleration amplitude spectra (the second time derivative of (2.23) using (2.18) and (2.7)) for Brune's and Hisada's slip velocity functions for two widths of the propagating pulse are presented in the figure 2.10. As we can see, the acceleration levels are a little higher than for the boxcar case (Fig. 2.7), however, they are lower comparing with the case of instantaneous slip (Fig. 2.3). To illustrate this, we show the amplification at high frequencies in the figure 2.11. Under the amplification we understand the term $C_d^2 X(aC_d)$, see Eq. (2.24).

To show the influence of the K-parameter in the slip distribution (2.7) on the acceleration spectrum, we display the acceleration spectra for the Hisada's slip velocity function for two values of L_0 and various K in Fig. 2.12.

2.2.4 Extrapolation to a rectangular fault

We derive formula for strong motion synthesis for given kinematic rupture model of a rectangular fault with the wave number dependent rise time.

We start with the representation theorem in the general form (1.6). We formally define the function

$$\boldsymbol{H}_1(\boldsymbol{r}, t; \boldsymbol{\xi}) = \boldsymbol{H}_0(\boldsymbol{r}; \boldsymbol{\xi}) \Delta(t - T(\boldsymbol{r}; \boldsymbol{\xi}) - t_r(\boldsymbol{\xi})), \tag{2.26}$$

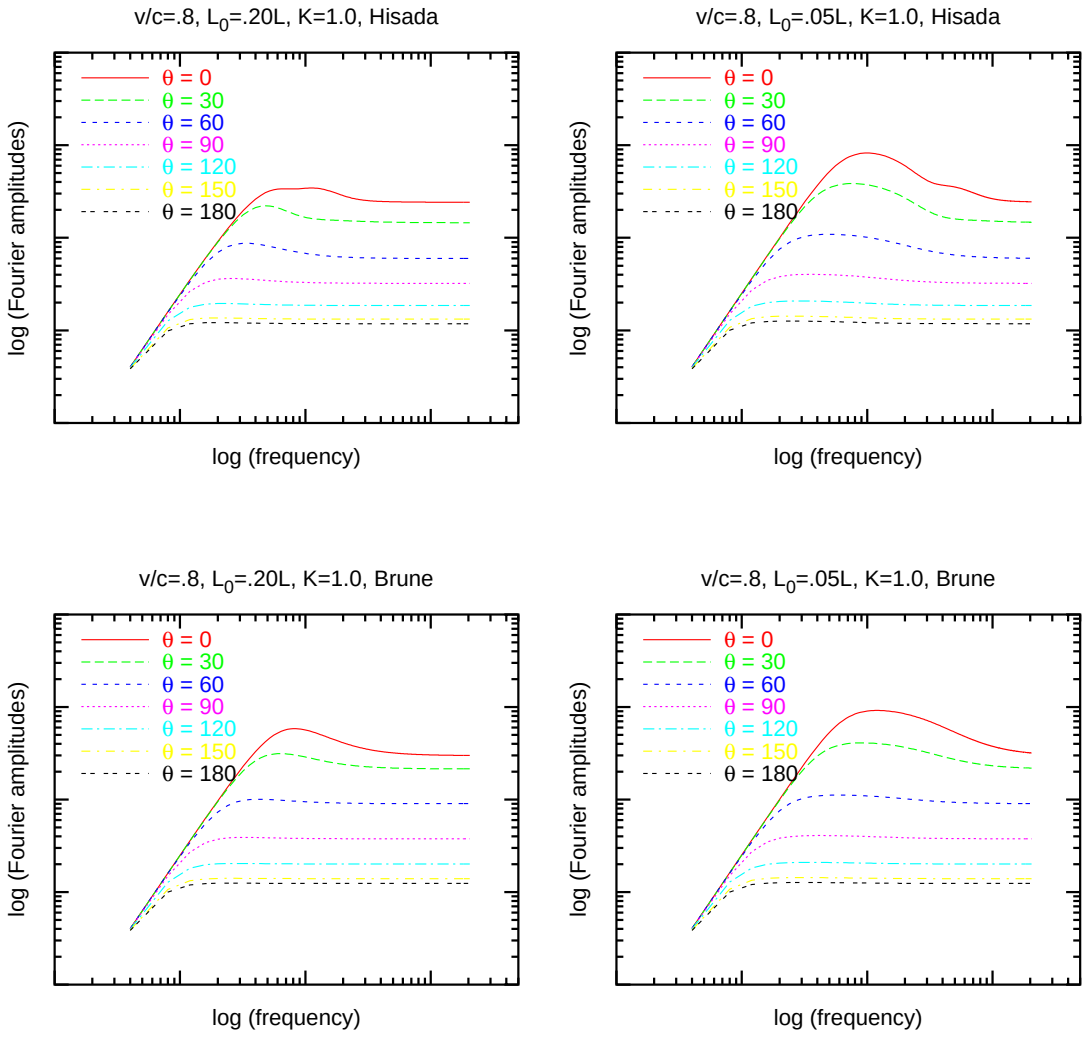

Figure 2.10: Amplitude spectra of acceleration generated by two different widths of propagating pulses (left and right) for two different slip velocity functions (top and bottom). The low, middle and high frequency effects are similar to the case of the boxcar slip velocity function in the figure 2.7. The ranges of axis are the same as in the figures 2.3 and 2.7.

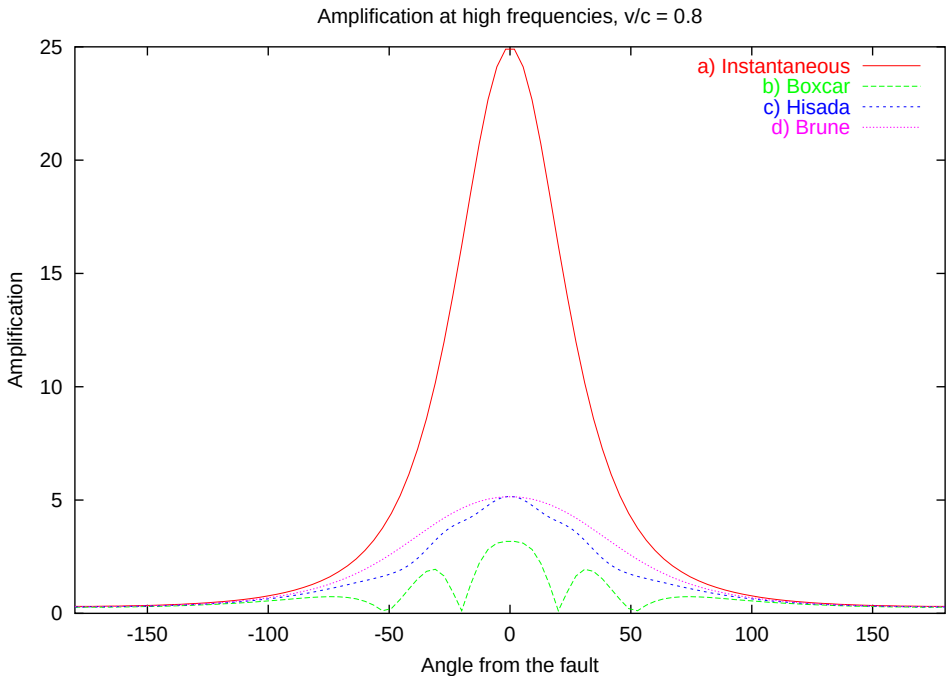

Figure 2.11: Azimuthal dependence of the amplification at high frequencies (high of the plateau of accelerogram's spectrum). a) Intantaneous: this graph shows the amplification for the kinematic model characterized by the k^{-2} slip distribution and the instantaneous slip. b), c), d) show functions which control high frequency radiation from k^{-2} dislocation with slip velocity functions boxcar, Hisada's, Brune's, respectively with rise time dependent on the wave number. Note that the oscillatory character of the amplification in the boxcar case is a consequence of its unrealistic shape. We avoid of the oscillations by assuming different (more realistic) slip velocity function.

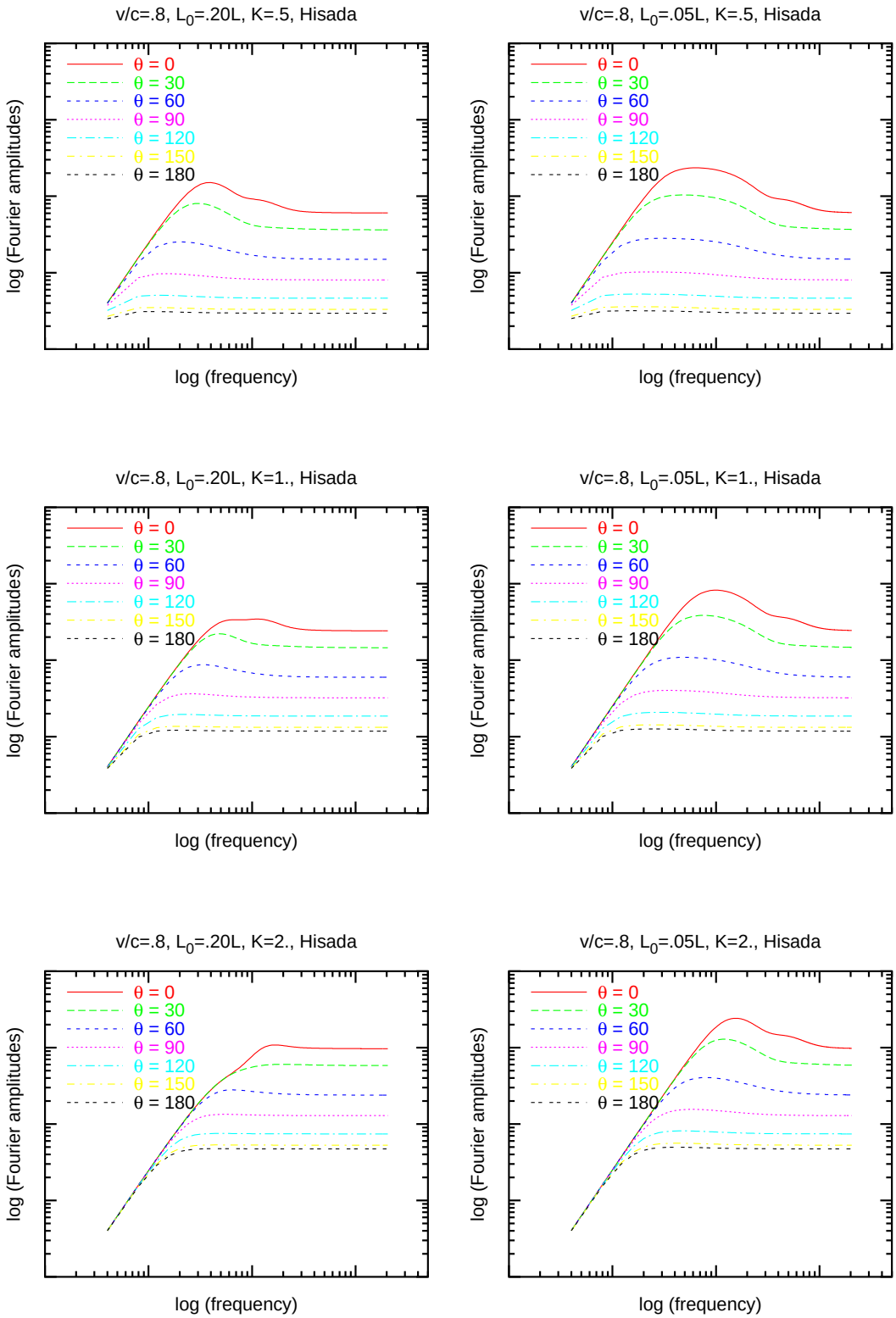

Figure 2.12: Amplitude spectra of acceleration for two widths of the propagating pulse (left, right) and for three K's (rows). The K-parameter strongly affects the radiated wave field since it changes K times the corner frequency and K^2 times the level of the acceleration spectral plateau.

where t_r is the rupture time. We take advantage of the definition of the time convolution and using (2.26) and (1.11) we can rewrite Eq. (1.6) in the following way:

$$\boldsymbol{u}(\boldsymbol{r},t) = \iint\limits_{\Sigma} d\boldsymbol{\xi} \boldsymbol{H}_1(\boldsymbol{r},t;\boldsymbol{\xi}) * [D(\boldsymbol{\xi})U(\boldsymbol{\xi},t)]\,. \tag{2.27}$$

Note that although we start with Eq. (1.6) derived for the ray approximation, $\boldsymbol{H}_1$ can represent also the time integral of the impulse response (given by, e.g., discrete wave number or finite differences method) shifted in time according to the rupture time.

As in the section 2.2.2, we assume that (2.27) was derived for the rupture process at given wave number $\boldsymbol{k}$:

$$\boldsymbol{u}(\boldsymbol{k};\boldsymbol{r},t) = \iint\limits_{\Sigma} d\boldsymbol{\xi} \boldsymbol{H}_1(\boldsymbol{r},t;\boldsymbol{\xi}) * [D(\boldsymbol{k};\boldsymbol{\xi})U(\boldsymbol{k};\boldsymbol{\xi},t)]\,. \tag{2.28}$$

To obtain the wave field generated by the rupture process at all wave numbers, we integrate (2.28) with respect to $\boldsymbol{k}$. Considering $D(\boldsymbol{k};\boldsymbol{\xi}) = D(\boldsymbol{k})e^{2\pi i \boldsymbol{k}\cdot\boldsymbol{\xi}}$ and rearranging terms in (2.28) we get

$$\boldsymbol{u}(\boldsymbol{r},t) = \iint\limits_{\Sigma} d\boldsymbol{\xi} \boldsymbol{H}_1(\boldsymbol{r},t;\boldsymbol{\xi}) * \left[\iint d\boldsymbol{k} D(\boldsymbol{k})U(\boldsymbol{k};\boldsymbol{\xi},t)e^{2\pi i \boldsymbol{k}\cdot\boldsymbol{\xi}}\right]. \tag{2.29}$$

For simplicity, we assume that, for given $\boldsymbol{k}$, the slip velocity function is the same for each rupture point (U does not depend on $\boldsymbol{\xi}$). As in Sec. 2.2.3, we assume that $U(\boldsymbol{k};t) = F(t/\tau(\boldsymbol{k}))/\tau(\boldsymbol{k})$, where $F(t)$ is a function of unit dislocation with one second duration. We put it in Eq. (2.29) obtaining

$$\boldsymbol{u}(\boldsymbol{r},t) = \iint\limits_{\Sigma} d\boldsymbol{\xi} \boldsymbol{H}_1(\boldsymbol{r},t;\boldsymbol{\xi}) * \left[\iint d\boldsymbol{k} D(\boldsymbol{k})\frac{1}{\tau(\boldsymbol{k})}F\left(\frac{t}{\tau(\boldsymbol{k})}\right)e^{2\pi i \boldsymbol{k}\cdot\boldsymbol{\xi}}\right]. \tag{2.30}$$

Note that the inverse spatial Fourier transform (the term in square brackets in Eq. (2.30)) gives for each point on the fault a unique slip velocity function. In other words, the slip velocity function is not more the same for each point on the fault because it is a sum of contributions from all wave numbers with wave number dependent rise time.

For numerical computations it is usually more convenient to transform Eq. (2.30) to the Fourier domain:

$$\boldsymbol{u}(\boldsymbol{r},f) = \iint\limits_{\Sigma} d\boldsymbol{\xi} \boldsymbol{H}_1(\boldsymbol{r},f;\boldsymbol{\xi}) \iint d\boldsymbol{k} D(\boldsymbol{k})X(f\tau(\boldsymbol{k}))e^{2\pi i \boldsymbol{k}\cdot\boldsymbol{\xi}}, \tag{2.31}$$

where $X(f)$ is the Fourier transform of $F(t)$.

We make following assumptions to generalize the k^{-2} rupture model for a 2D finite fault. The rupture propagates radially at constant velocity v. The rise time distribution is radially symmetric:

$$\tau(\boldsymbol{k}) = \frac{\tau_{max}}{\sqrt{1 + \left(\frac{L_0 k}{a}\right)^2}}, \quad k = |\boldsymbol{k}|. \tag{2.32}$$

The generalization of the slip distribution is discussed in detail in the appendix A.

The above mentioned assumptions allow for computation of the slip functions for a finite rectangular fault. The problem which still remains is the computation of Green's functions. It is discussed in next section.

Chapter 3

Strong motion synthesis

The Earth's structure is very complex since it includes 3D small-scale heterogeneities and attenuative and local topographical properties. These complexities cannot be studied deterministically (e.g., by any geophysical measurements), nevertheless, they are important for signals at high frequencies.

The propagation of seismic waves in media with statistically varying velocities at small scales was modelled by finite differences by *Frankel and Clayton*, 1986. They showed that such perturbations in velocities can explain observed high frequency effects like travel time variations across large-scale seismic arrays, coda waves and backscattered coda waves and their time decay, etc. On the other hand, these effects are not strong enough for buried fault in the near source region to be responsible for the largest peaks on accelerograms.

The strong motion array analyses show that high frequency (> 1Hz) content of the wave-fields is incoherent. To solve this problem, *Abrahamson and Bolt*, 1987 suggested to generate a number of synthetic ground motions with statistically varying Fourier phase for the incoherent energy. In other words, while the deterministic approach seems to be unable to handle the problem, the stochastic approach (e.g., fractal) should be preferred.

The dynamic rupture properties (static and dynamic frictional coefficients, strength) needed in the fault mechanics are complex as well as the seismic wave propagation. In our study, we assume that the stochastic nature of acceleration records at high frequencies can be involved into the source and that, consequently, the deterministic computation of propagation effects is sufficient.

In this chapter, we discus the computation of Green's functions needed in the kinematic strong motion synthesis.

3.1 Ray theory

High frequency accelerograms may be computed using the ray theory (more precisely, the zero-order term). The ray approach gives, in principle, only the far-field

term of the complete Green's function. This technique is applicable to general 3D heterogeneous structures.

The ray theory is very efficient for computation of high frequency wave-fields since we can obtain from a solution for one frequency the values for other frequencies at nearly no cost. It is due to the advantage of using the fast frequency response algorithm (see *Červený*, 1985).

This method is much faster (for reasonable number of rays) than the other methods for computing full wave fields (discrete wave numbers, finite differences, etc.). The disadvantage is that it omits near-field term, surface waves, head waves and all others non-geometrical waves (pseudospherical waves, leaking waves, etc.).

The ray theory (*Červený et al.*, 1977) gives a formula for the amplitude of the impulse response of general medium (see Eq. (1.5)) calculated along one ray connecting the source with the station:

$$\boldsymbol{H}_0(\boldsymbol{r};\boldsymbol{\xi}) = \frac{\mu(\boldsymbol{\xi})\boldsymbol{F}^c(\boldsymbol{r};\boldsymbol{\xi})}{4\pi\rho(\boldsymbol{\xi})c(\boldsymbol{\xi})^3}\left(\frac{\rho(\boldsymbol{\xi})c(\boldsymbol{\xi})}{\rho(\boldsymbol{r})c(\boldsymbol{r})J(\boldsymbol{r};\boldsymbol{\xi})}\right)^{\frac{1}{2}}\Pi(\boldsymbol{r};\boldsymbol{\xi}), \tag{3.1}$$

where ρ is the density, c either P or S wave velocity, $\sqrt{J}$ denotes the geometrical spreading and $\boldsymbol{F}^c$ the radiation pattern depending on the takeoff angles of the ray at the source and the geometrical properties of the fault (strike, dip, rake). Π is the product of all reflection and transmission coefficients at the interfaces impinged by the ray along its trajectory. The other quantities are defined in chapter 1.2.

It should be noted that $\boldsymbol{H}_0$ is generally complex since J can be negative (when the ray passes caustics) and Π can contain non-zero imaginary part when the ray is reflected or transmitted at a supercritical angle.

To compute the ray solution according to (3.1), we need to find rays connecting the source with the station. They can be found by solving the ray tracing system. The ray parameters (initial conditions, e.g. two take-off angles in 3D) can be found for simple medium analytically by Snell's law. A numerical approach is necessary for more complicated media.

In our study, two step method for the two point ray tracing is used. The azimuth of the ray is changed until the ray ends on a profile that connects the centre of the coordinate system with the receiver. For such rays, classical regula-falsi method is used to aim the receiver, i.e, to find the proper azimuth and declination. Π and the propagation time are easy to compute for known ray trajectory. The dynamic ray tracing system is solved along the ray to obtain the geometrical spreading.

Having all the necessary quantities for (3.1) and the propagation time, we can compute, for given slip velocity function, the synthetic seismogram for one elementary wave. The final seismogram is a superposition of contributions from all elementary waves.

Since we are interested in ground shaking acceleration maps, we assume a set of receivers radially distributed on profiles going from the centre of the coordinate system. The computation of ray synthetic seismogram is performed according to following steps.

- The fault is covered (represented) by a grid of point sources.
- All rays connecting the source points and the receivers for each elementary wave are found and all parameters of the ray solution (the amplitudes and the propagation times) are obtained.
- Synthetic spectra of seismograms for each point source are computed by the product of the slip velocity spectrum with the spectrum of the sum of (1.5) using (3.1) for each elementary wave.
- Spectra are multiplied by $(i\omega)^2$ and the inverse Fourier transform is performed to obtain the ray synthetic accelerograms.
- For a finite fault all contributions from point sources over the fault properly shifted in time with respect to the rupture time are summed.

We have to remember that computation of the wave-field is efficient only for a reasonable set of rays.The problem is that it is necessary to assume for kinematic modelling a large number of point sources distributed over the fault because we need to evaluate numerically the integral of representation theorem. This problem is well discussed in *Spudich and Archuleta*, 1987. There the authors show that the impulse responses (as functions of spatial co-ordinates on the fault) and the slip distributions have to be sampled sufficiently at shortest wavelength λ connected with the lowest velocity v and the highest computed frequency f ($\lambda = v/f$) in the modelling. It is also shown that the sampling has to be denser for a receiver in the opposite direction to the direction of rupture propagation (at least 6 point sources per the wavelength) than for a receiver on the other side (about 3 samples per the wavelength). Note that the understanding of the latter effect can be found also in equation (2.6). The Nyquist wave number of the fault sampling has to be higher than the maximum k_x in (2.6) corresponding to the highest computed frequency and the lowest C_d (i.e., for the opposite direction of the rupture propagation, see figure 2.4).

For example, we have to sample a relatively small fault of dimension 5×4 km by at least 32×32 of point sources when computing up to 5Hz for a station located in the direction of the rupture propagation. We have 1024 sources, multiplying by e.g. 80 stations, we obtain 81920 rays for each code! It is very high number since the ray tracing is relatively very time-consuming.

Thus, we have to find a way to reduce the number of necessary rays.

3.2 Direct S-waves

We discussed in the introduction to this chapter that the wave propagation is rather complex. However, it is common opinion in seismological literature (e.g., *Hanks*, 1982, *Zollo et al.*, 1997, *Emolo and Zollo*, 2001) that the most damaging high frequency waves for receivers closer than about 50km from a *buried* fault are the direct S-waves. The other elementary waves (e.g., reflected from MOHO) become important in larger epicentral distances (*Gasperini*, 2001). On the other hand, the fault that reaches the surface is more likely to generate strong surface waves. All types of waves can be then trapped in basin structures causing larger damages.

Because we will perform strong motion synthesis for a fault that is located about 7km beneath the surface, we assume that computation of only direct S-waves in the wave-field gives reasonable estimates of peak ground acceleration (PGA). Moreover, it obviously results in faster computation. Other methods should be used to predict other quantities important in earthquake strong motion prediction like duration magnitude, which would be rather underestimated, or root mean square acceleration (a_{rms}), which would be overestimated. In our text we will be concerned mainly with PGA as one of the most common quantity (besides, e.g., the response spectra), which has been studied also empirically (see appendix A.3) and can be roughly related to macroseismic data (intensities). It allows our computations to be compared with measurements.

To test our assumption, we calculate three-component accelerograms from a point source located in the depth of 12km by two methods: by the ray theory in a layered medium assuming direct S-waves only and by the discrete wave number (DWN) method which gives full wave-field solution (see figure 3.1). Note the good fit of peak amplitudes. Of course, the lengths of the accelerograms differ.

For the second test we use accelerograms modelled also by the two methods mentioned above for a 5×4 km Haskel's fault (see figure 3.2). Again, a reasonable fit for PGA estimates is obtained. It gives us hope that the PGA maps computed for direct S-waves only (in chapter 4) will represent reliable results.

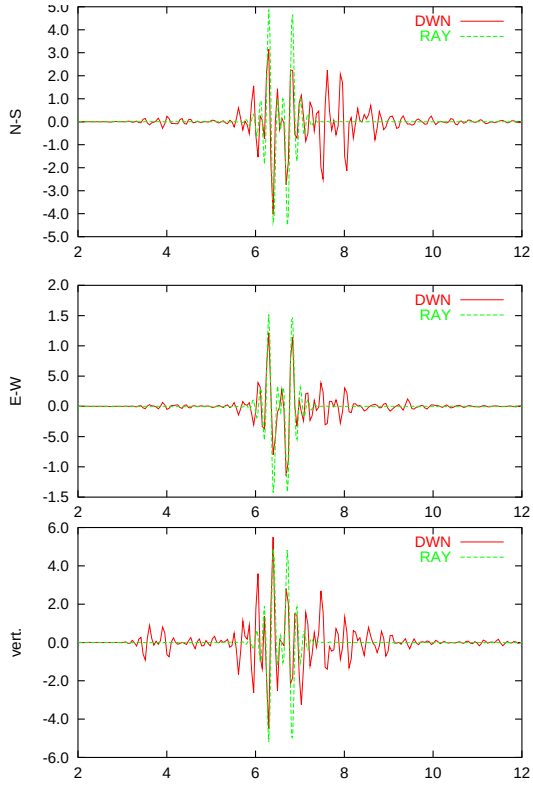

Figure 3.1: The three-component synthetic accelerograms generated by a buried point double-couple source (12km depth). The direct S-wave fits PGA of the full wave field well.

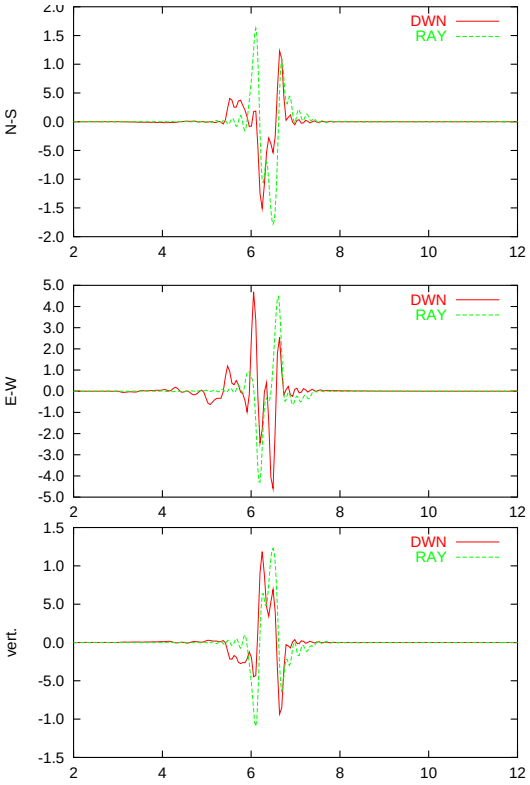

Figure 3.2: The three-component synthetic accelerograms for a receiver in the direction of rupture propagation generated by a buried Haskell fault with radial (instead of unilateral) rupture propagation. The direct S-wave is clearly responsible for the PGA of the full wave field.

3.3 Interpolation

Let us discuss the interpolation methods used to reduce the number of necessary Green's functions needed for kinematic modelling.

There are several ways how to interpolate the impulse responses of a medium. The easiest one is to find only one Green's function (usually for the centre of the fault). The Green's functions for remaining points on the fault are then obtained by shifting in the time domain with respect to the hypothetical propagation time of S waves in homogeneous medium surrounding the fault. The amplitude is corrected by considering the proper geometrical spreading. This approach is well known in the Empirical Green's Function (EGF) method. There, dispite of such rough approximation, we can obtain relatively good results thanks to the realistic impulse response involved in the computation. Nevertheless, it is obvious that it provides a reasonable approximation in regional distances. On the other hand, it could cause large errors in near source region.

The more accurate method is to find the Green's functions from a sparse grid of point sources on the fault and to use some of the interpolation techniques discussed, for example, in *Spudich and Archuleta*, 1987. They can be split into two groups: time domain and Fourier domain approaches. In the time domain techniques, the spatially adjacent impulse responses are shifted in time like in one Green's function case and linearly weighted with respect to the time shift. Again, these interpolation techniques assume the S wave to be the only significant arrival. The Fourier domain techniques are based on an assumption that the Green's functions are basically oscillatory functions of position with wavelengths corresponding to c/f. It means that Green's function at given frequency as a function of coordinates on the fault can be refined from a sparse grid to a dense grid by, e. g., bicubic splines. However, the sparse grid still has to be dense enough to "see" the shortest wavelengths, thus we still have to find relatively large number of Green's functions.

These techniques are very time-consuming because the procedures have to be performed for each combination of time/frequency and station. Their use is beyond the scope of this text.

In this work we take advantage of the zero-order ray solutions. They are determined by three parameters for each ray: the arrival time, the real and the imaginary part of the amplitude. Only these quantities have to be interpolated for each combination of elementary wave and station which results in faster computation of medium impulse responses. Moreover, the changes of that parameters of the ray solution with respect to position on the fault are usually smooth in, e. g., medium consisting of homogeneous layers. It allows for using bicubic splines as interpolation functions. The interpolation is performed on a rectangular grid. The values are interpolated first in one direction and then the resulting parameters are interpolated in the second direction.

An example of accelerograms computed for the same fault model as in the

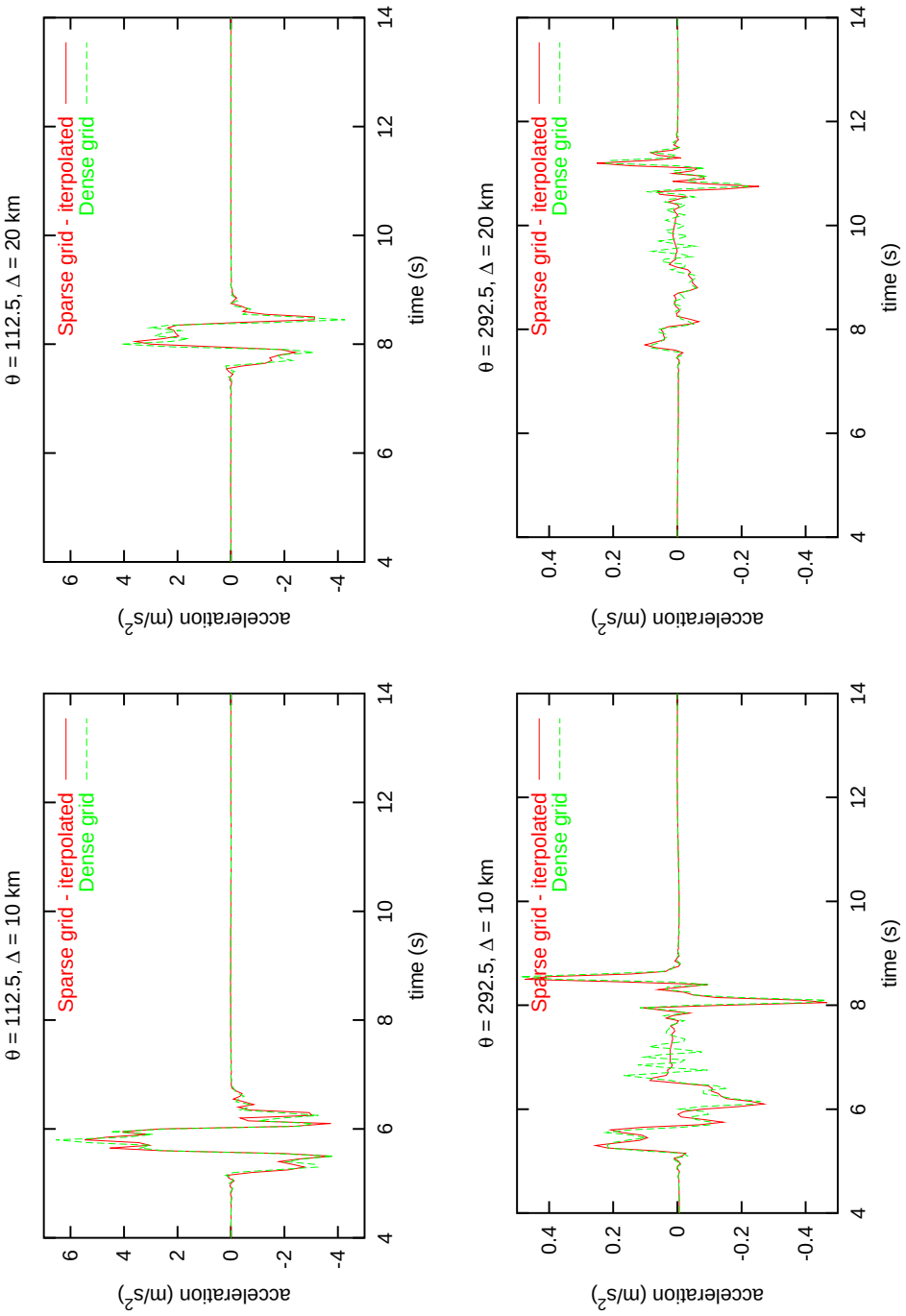

Figure 3.3: A comparison of synthetic accelerograms computed for a finite fault assuming only direct S waves in layered medium. The stations are located in the direction of rupture propagation (bottom) and in the opposite direction (top) in two epicentral distances of 10km (left) and 20km (right). The number of rays found for each station is 32×32 (dense) and 8×8 (sparse) whose parameters of the ray solutions are interpolated into a grid 32×32. Note that the accelerograms consist of the starting and stopping phases caused by the edges of the fault in Haskell model.

previous section can be found in the figure 3.3, where ray solutions for only 8×8 point sources are interpolated into a sufficiently dense grid 32×32. It results in about 16 times faster evaluation of impulse responses (the time necessary for interpolation is negligible). The example clearly shows a good agreement in the direction of rupture propagation. In the opposite direction the accelerograms noted as "dense" exhibit artificial oscillations between the starting and stopping phases unlike the accelerograms noted as "sparse". This "ringing" effect is an effect of slight spatial undersampling of the fault (*Spudich and Archuleta*, 1987). The reason why it is not present in the case of a sparse grid is that the interpolation smoothes the behaviour of Green's functions over the fault. In this case, the interpolation smoothes the result that it looks better than the ringing wave which of course does not mean that it is more accurate.

The interpolation provides a way to minimize the time needed for the Green's functions computation. It should be emphasised that dense grid necessary for high frequency computations still makes the problem very time-consuming due to the summation of contributions from all point sources.

Chapter 4

Application of the k^{-2} rupture model to the 1999 Athens earthquake

The Athens earthquake in the area of Attica on September 7, 1999 at 11:56:50 GMT surprised seismologists with its $M_w = 5.9$ since no seismological data (historical records, instrumental data) have shown evidence of events with magnitude $M_w > 5$ at distances smaller than 30km from Athens. The maximum intensity was determined XIII-IX in the NW outskirts of Athens. In the area, the earthquake caused death of 143 people and injuries for more than 2,000.

Fortunately, the rupture process did not reach the surface and stopped at the depth of about 7 kilometers. It resulted in relatively short strongest ground motion phase (predominantly direct S waves).

In the Attica region, there are two nearby N120^o-130^o south dipping normal geological faults (Fili and Aspropyrgos) which are about 10km distant from each other. The seismologists have not yet been able to determine definitely which of these faults was activated, although the Fili fault seems to be more probable.

The location and focal mechanism were determined by a number of seismological agencies (National Observatory of Athens – NOA, U.S. Geological Survey – USGS NEIC, Harvard, Geophysical Laboratory of the Thessaloniki University and others). The locations of epicentre are in a range of 38.02^o-38.15^o N and 23.55^o-23.71^o E. In our text, we consider the coordinates of epicentre 38.08^o N and 23.58^o E (NOA, after relocation) fixed.

It is not surprising that the source depth determination did not give consistent results (from 9 to 30km). The result of ASPO method (*Zahradník* (submitted)), 12km, is used in this work as the most reliable because it takes into account first motion polarities as well as the amplitude spectra of complete regional seismograms.

The focal mechanisms, determined by different agencies, seem to be quite consistent (for review see *Tselentis and Zahradník*, 2000a, b). We fix the so-

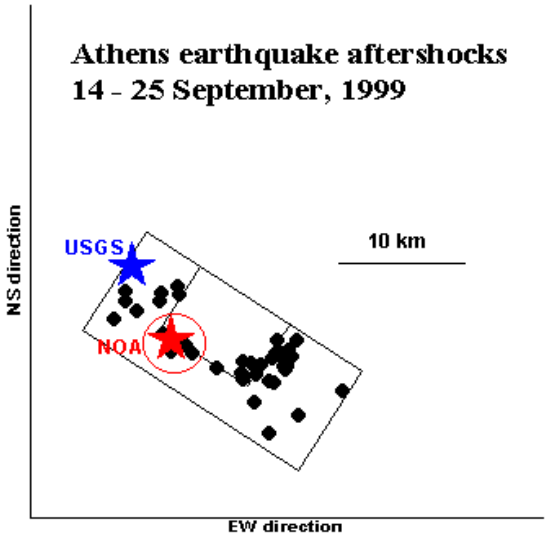

Figure 4.1: The map view of September 14-25, 1999 aftershocks (full circles) and two alternative faults proposed by *Tselentis and Zahradník*, 2000a, b. The USGS-NEIC and NOA (relocated) epicentres are presented. The locations of the epicentre with respect to the position of both suggested planes agrees with observed directivity of the earthquake (see the text). After *Zahradník and Tselentis* (submitted).

lution given by USGS-NEIC: strike 123^o, dip 55^o and rake -84^o. The identification of the main shock fault plane with one of the two nodal planes has been confirmed by the recognition of aftershock spatial clustering (*Tselentis and Zahradník*, 2000a, b). Moreover, it is consistent with the orientation of the geological faults mentioned above.

The fault plane solution given by *Kontoes et al.*, 2000, based on satellite radar interferometry (SAR), quite differs. They proposed also a secondary parallel shallow fault plane with the strike of 96^o and the dip of 40.9^o to model the asymmetry observed in the SAR interferogram. This secondary fault is neglected in this study.

The spatial distribution of aftershock epicentres suggests two possible dimensions of faults (see figure 4.1): 20×16 km with the assumption that the strain on the fault was not fully released and the remaining strain was relieved by aftershocks; 8×10 km with the assumption that the main shock released complete strain and the aftershocks occurred in the surroundings[1] (*Tselentis and Zahradník*, 2000a, b).

Plicka and Zahradník (submitted) inverted regional data from 7 broadband stations by the EGF method to obtain the position of the fault with respect to the fixed hypocentre position (assumed to be the position of the nucleation point on the rupture). The authors suggest that the nucleation point is located on the western edge of the fault. Thus, the rupture propagated mainly in the strike direction, towards Athens. It resulted in strong directivity effect in that

[1]It should be noted that the studied aftershocks occurred within 12 days, starting 7 days after the main shock. Exact location of the aftershocks that occured earlier after the main shock is unknown.

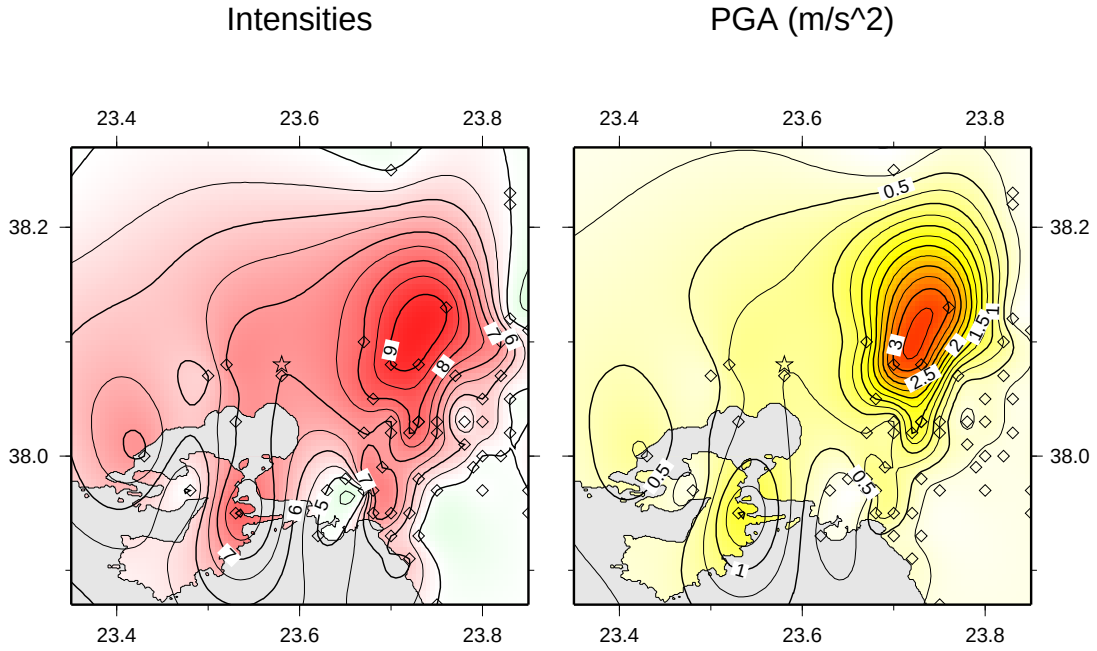

Figure 4.2: Observed intensities I (left) published by NOA and PGA map (right) computed according to mean values in table 4.1 with about 30% variance. The maps arise from interpolation of values at data points, which are represented by diamonds in the maps. The star denotes the relocated NOA epicentre.

direction. It has been confirmed by macroseismic data (intensities, see figure 4.2), published by NOA, as well as by the shapes of apparent source time functions studied by *Baumont et al.* (submitted). In this case, the effect of directivity seems to be responsible for the large losses. Now we can understand why such moderate size earthquakes represent a very serious seismic hazard in areas like Europe (especially Greece and Italy).

The EGF modelling in the paper by *Plicka and Zahradník* (submitted) was not able to resolve the dimension of the fault (i.e., to decide which one of the above mentioned fault model is more likely).

The fault dimension 7.5×6 km was found plausible by *Zahradník and Tselentis* (submitted) to generate realistic PGA's (see figure 4.3). The authors used a hybrid method (so-called PEXT method), which is based on deterministic modelling of generated wave-field up to a frequency a little higher than the corner frequency. The flat part of the acceleration spectrum behind the corner frequency is extrapolated by a spectrum of a stochastic white noise. In the deterministic part of the method, the composite modelling with equally sized subevents with spatially constant slip is used.

In our study, we relax the assumption of constant slip. The main aim is to constrain values of kinematic parameters of the k^{-2} rupture model (see section

Intensity	$a(cm/s^2)$
V	12 – 25
VI	25 – 50
VII	50 – 100
VIII	100 – 200
IX	200 – 400
X	400 – 800

Table 4.1: The empirical relation between the macroseismic intensity and PGA. After *Willmore*, 1979.

Lat. (N)	38.08^o
Long. (E)	23.58^o
Depth (km)	12.0
Moment (Nm)	$7.8 \cdot 10^{17}$
Strike	123^o
Dip	55^o
Rake	-84^o
v (km/s)	2.8

Table 4.2: Fixed parameters for the Athens earhquake model. Note, v is the radial rupture velocity.

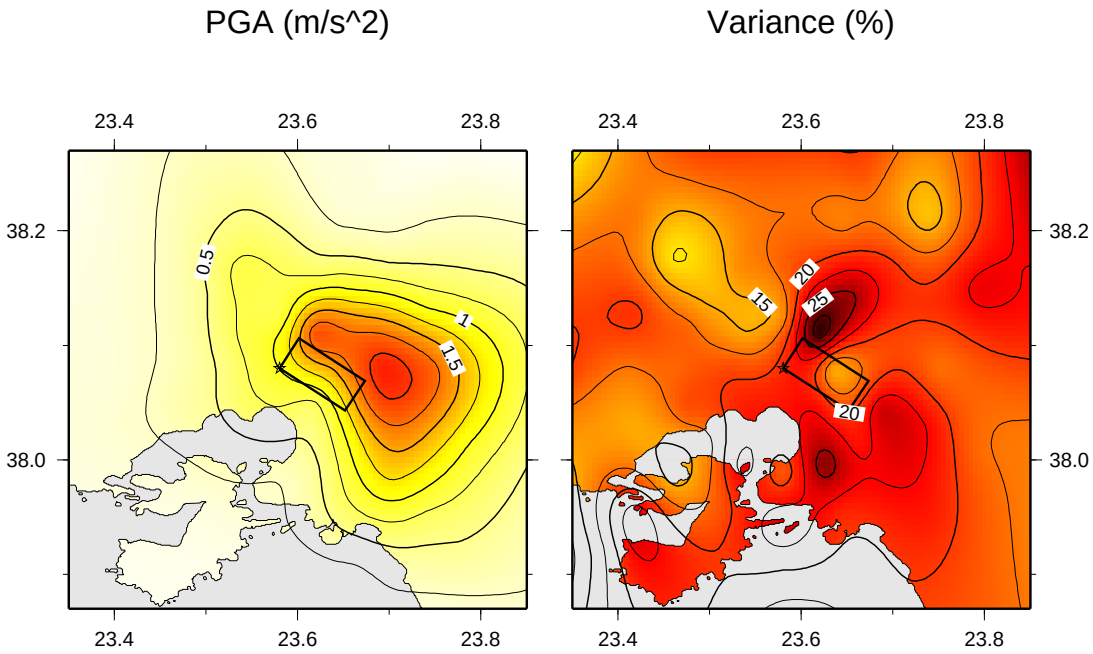

Figure 4.3: PEXT simulation of the Athens earthquake with 7.5×6 km fault under the assumption of homogeneous slip. The rectangle represents the projection of the fault on the earth's surface. The star represents the epicentre (NOA, relocated). Modified from *Zahradník and Tselentis* (submitted).

thickness (km)	$v_p(km/s)$	$v_s(km/s)$	$\rho(g/cm^3)$
1	2.67	1.50	2.50
1	4.45	2.50	2.50
3	5.70	3.20	2.84
13	6.00	3.37	2.90
21	6.40	3.60	2.98
∞	7.90	4.44	3.28

Table 4.3: Parameters of crustal model MA.

2.2). We study the influence of L, W, L_0, K and the shape of the slip velocity function on the PGA maps. In this text, we want to restrict the range of possible values of these parameters by comparison with the observed data (Fig. 4.2). We try to find a set of suitable k^{-2} models for the Athens earthquake.

4.1 Computational details

The fixed parameters of the Athens earthquake model are listed in the table 4.2. We assume that the nucleation point (located in the bottom left corner of the fault) corresponds to the hypocentre. The rupture propagates radially at constant rupture velocity v.

The crustal model, called MA, used for discrete wave number modelling of regional data by *Tselentis and Zahradník, 2000b*, was chosen for our computations. This 1D structural model consists of homogeneous layers described in the table 4.3. The uppermost 1 km low-velocity layer is partly confirmed by, e.g., the surface waves dispersion study in *Novotný et al.*, 2001. Since the direct S waves represent the most important part of the generated wave field in terms of amplitudes of accelerograms, only these waves are taken into account.

The computer code for 2D ray computations BEAM87 written by Červený and modified by *Brokešová*, 1993, to allow for 2.5D computations is used. Under the 2.5D computation we understand computation of 3D rays in 2D medium (i.e., medium with properties dependent on vertical and one horizontal coordinate, in general). In the case of the adopted crustal model, we do not take advantage of the code fully since the crustal model is 1D only. On the other hand, we need 3D rays because of the 3D position configuration of the sources/receivers. Note also that neither topography nor site effects are taken into account. Thus, our results correspond rather to seismograms on the bedrock. To allow for site effects, the synthetics can be further convolved with local amplification functions.

In our computation we consider the frequency range up to 5.5Hz believing that f_{max} is somewhat higher in the Athens region. The attenuation effects are

neglected. The high frequency randomness of wave propagation could be assumed to be formally involved in the randomness of the k^{-2} source. The incoherent nature of high frequency waves (due to propagation) is neglected because then the comparisons of results are more clear. Both the last mentioned effects are discussed in the begining of Chap. 3.

To produce the maps of PGA values around the fault, the receivers are radially distributed on 16 line profiles, intersecting at the epicenter, with azimuthal increment of 22.5^o. On each profile, there are 5 receivers at the epicentral distances of 5 – 25 km, step 5 km. The horizontal PGA's computed at these receivers are used to generate desired PGA maps by interpolation. Under the horizontal PGA we understand the magnitude of the vectorial sum of both horizontal components. All maps are displayed in the same section of Greece as the empirical data shown in the figure 4.2.

4.2 5×4 km fault model

We start with probably underestimated dimension of the fault (compare with results of the previous studies) and show that it provides unrealistic results. Let us assume $K = 1$ (see Appendix A).

Figure 4.4 shows PGA maps generated by k^{-2} rupture model with instantaneous and wave number dependent rise time ($L_0 = 0.2L$, boxcar slip velocity function) for two different realizations of final slip on the fault. The bottom part of the figure shows the mean PGA map of 100 realizations. The map of variance for the case of k-dependent rise time is on the right in the figure 4.5. The variance is about $20 - 30\%$ everywhere and does not exhibit any systematic behavior with respect to the position of the fault or directivity.

As we can see from the figure 4.4, in all cases the position of the area of highest PGA is in the east direction from the epicentre. It is a consequence of the combination of the directivity effect and the S wave radiation pattern. To enlighten the effect of the latter, the figure 4.6 shows how the PGA map changes when the double couple radiation pattern is neglected (isotropic radiation from each point source is considered).

Qualitatively, the mean map (see Fig. 4.4) indicates that the differences between the maps for different slip distributions (in the same figure) are rather two extremes. The top one has the PGA focused in one point on the surface while the middle has the PGA maximum rather split in two adjacent areas. Substitution of instantaneous to k-dependent rise time changes a bit the shape and position of the high PGA area but the map qualitatively remains the same.

The values predicted by the model with instantaneous rise time are more than 5 times higher than those simulated by the model with wave number dependent rise time. It has been explained for a line fault in the Fraunhoffer's approximation (see the figure 1.1). The PGA values for the instantaneous rise time are more than

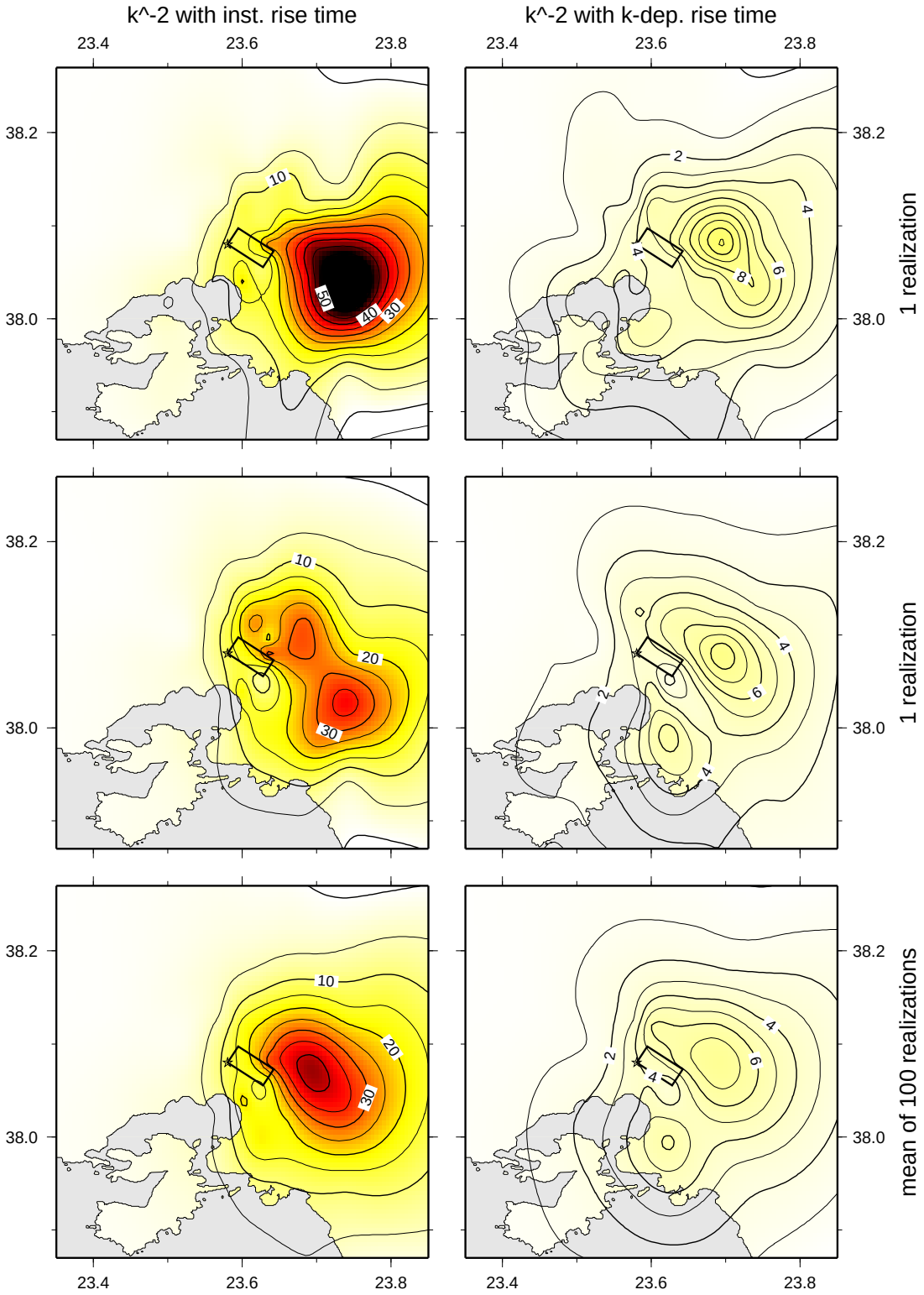

Figure 4.4: PGA maps in m/s^2 for instantaneous (left) and wave number dependent (right) rise time ($L_0 = 0.20L$) for the fault dimensions 5×4 km. In the top and the middle part the figure shows results for two different realizations of the slip distribution. The mean result of 100 realizations is shown in the bottom. The rectangle in the middle of each map represents the projection of the fault to the earth's surface. The star denotes the epicentre.

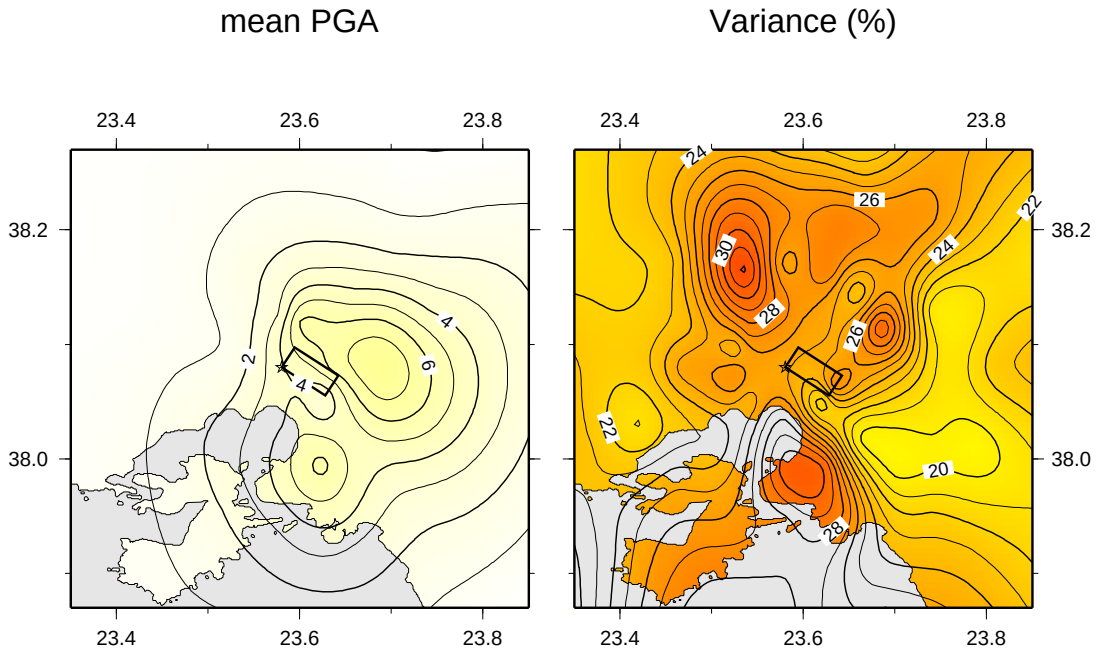

Figure 4.5: The mean PGA map in m/s^2 (adopted from the figure 4.4) for wave number dependent rise time (left) and its variance map (right). The fault is projected onto the surface. The star denotes the epicentre.

50 times higher in the direction of the rupture propagation than in the opposite direction. Such strong directivity effect has never been measured. That's why this model was revised by *Bernard et al.*, 1996, and the k-dependent rise time was introduced.

On the other hand, the k^{-2} rupture model with instantaneous rise time was succesfully used for strong motion prediction by, e.g., *Zollo et al.*, 1997 and *Emolo and Zollo*, 2001. Their mean predicted values of PGA do not seem to be unrealistic because they compute the means from results obtained for varying nucleation point position on the fault. Note that if we put the nucleation point on the opposite side of the fault (bottom right), the area of highest PGA would move to the opposite side with respect to the fault. The mean values would be then much lower, hence providing "realistic" estimates. However, their variances are very large (somewhere reaching 100%).

Although the k-dependent rise time gives lower PGA values, it is obvious that they are still overestimated. We should investigate whether the change of the slip velocity function would make any difference.

Results for different combinations of two widths of the slip pulse ($L_0 = 0.20L$ and $L_0 = 0.05L$) and three types of slip velocity functions (boxcar, Hisada's and Brune's, see the figure 2.9) are shown in the figure 4.8. The used slip distribution is the same as for the first realization in the figure 4.4.

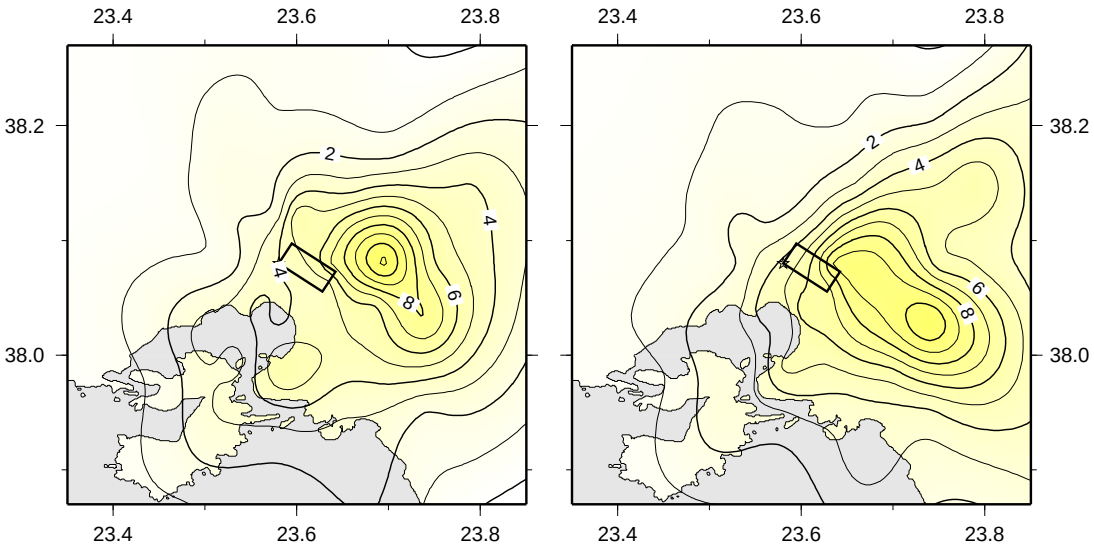

Figure 4.6: The influence of the S wave radiation pattern (see Fig. 4.7) of the Athens earthquake on the PGA maps: the radiation pattern is taken into account (left, the same as in Fig. 4.4 top right) and it is neglected (right). The right map is scaled by the largest value of PGA on the left figure.

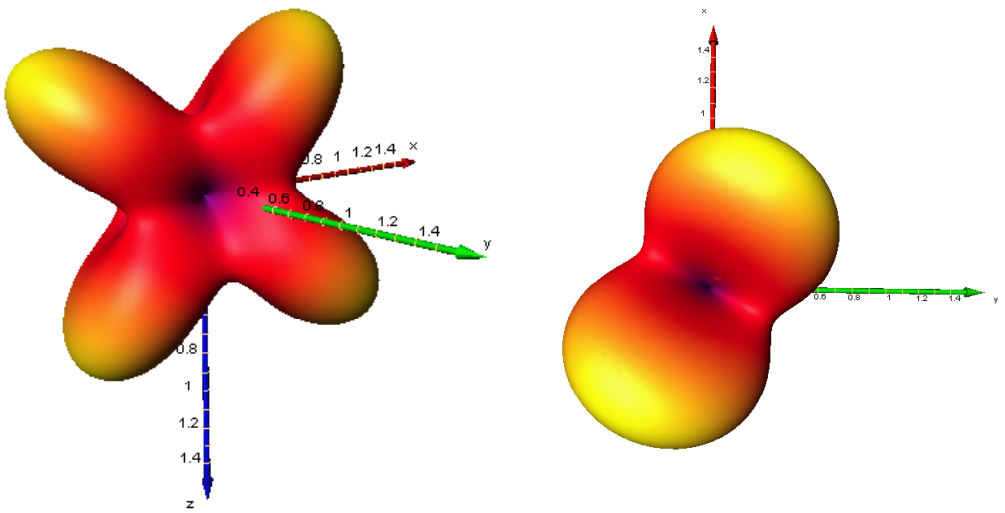

Figure 4.7: The figures show the used S wave radiation pattern (square root of the sum of SH and SV radiation patterns squared) in two different view angles. The x-axis goes to the north, the y-axis to the east.

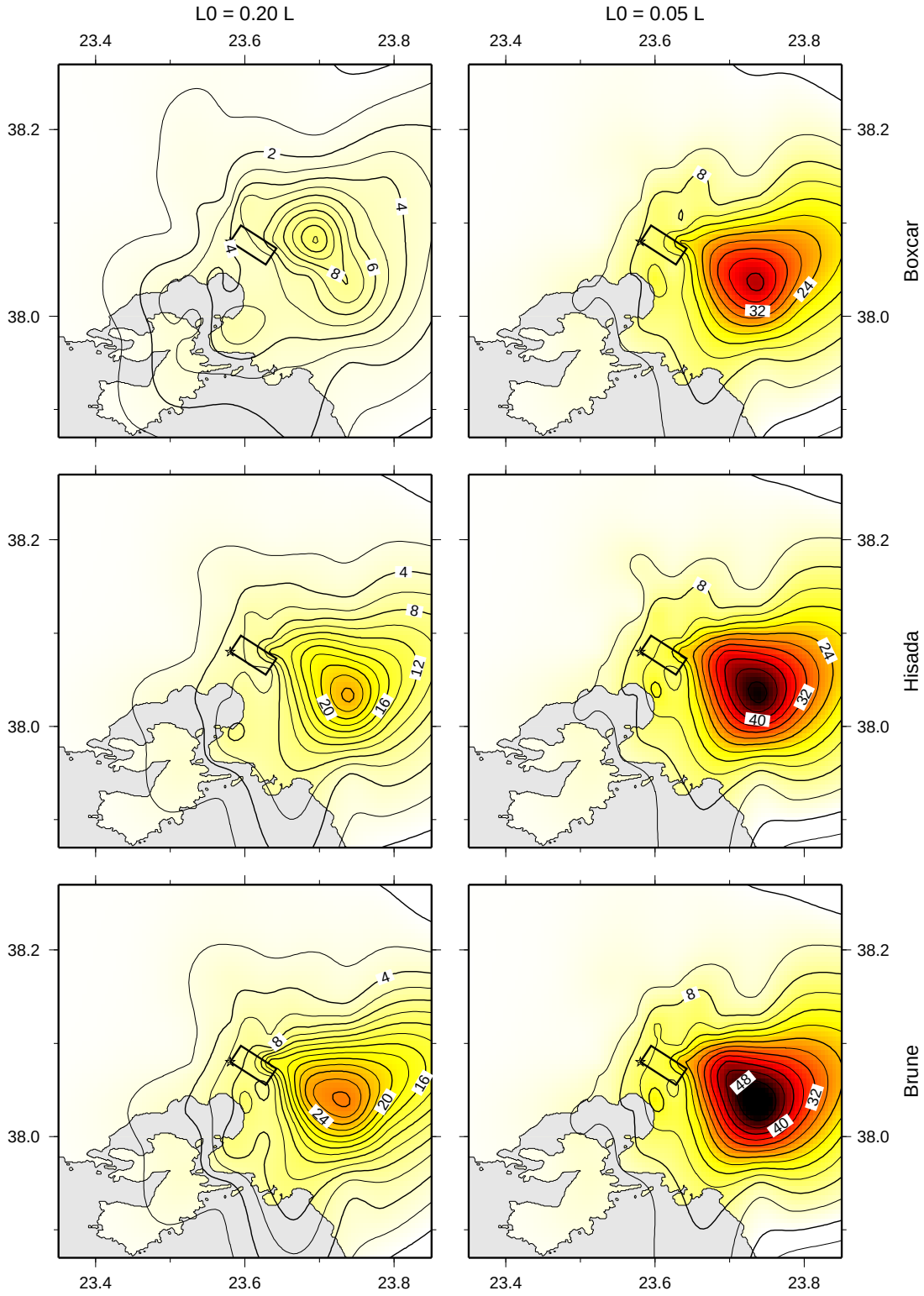

Figure 4.8: PGA maps in m/s^2 for two slip pulse widths ($0.20L$ and $0.05L$) and three slip velocity functions. The slip distribution is the same as was used for the maps in the top of the figure 4.4. The position and the size of the fault is the same as in the figure 4.4.

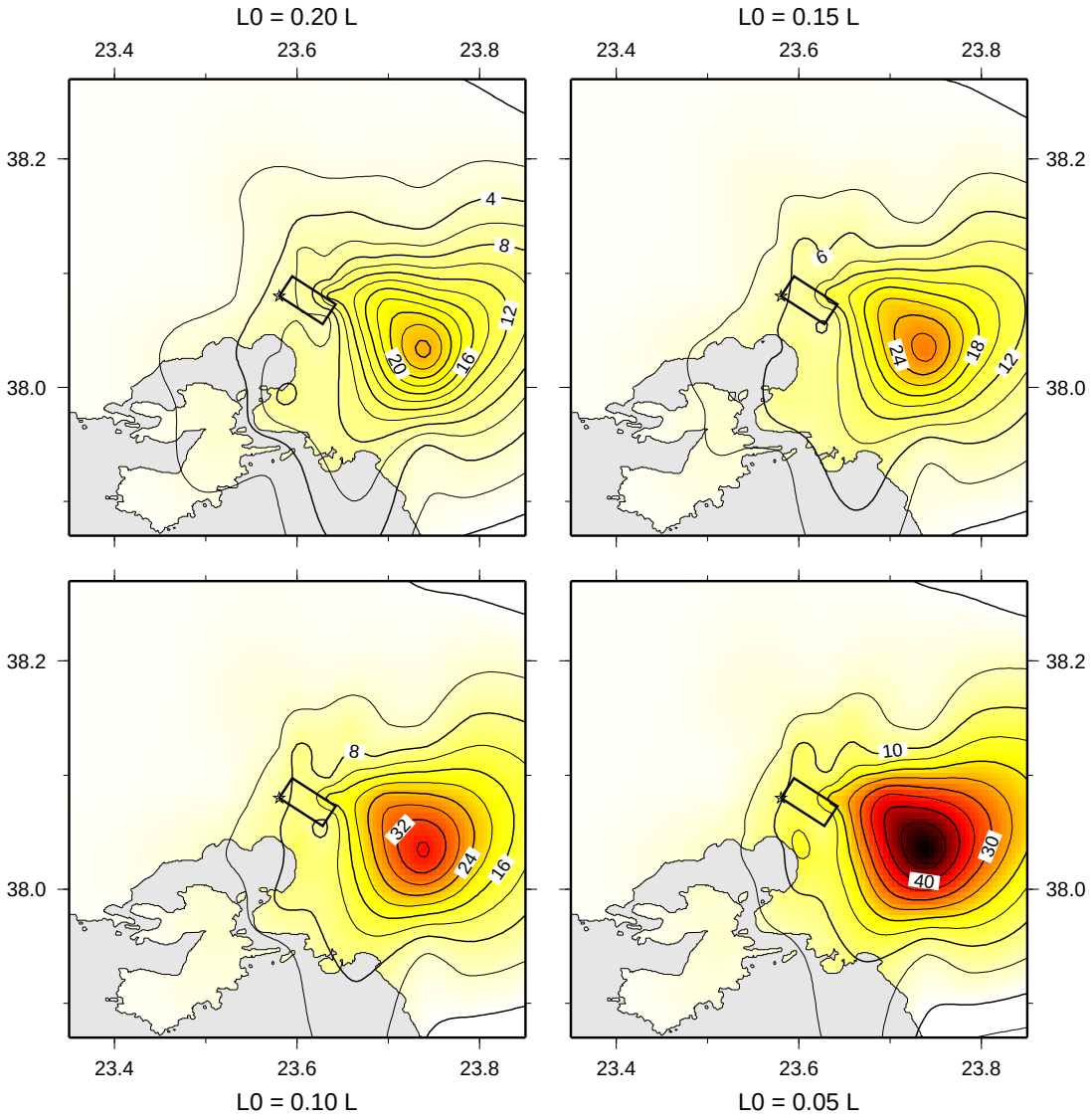

Figure 4.9: PGA maps in m/s^2 illustrating the influence of the pulse width from $L_0 = 0.05L$ to $L_0 = 0.20L$. The slip distribution is the same as was used in the figure 4.8. The Hisada's slip velocity function is used. The position and the size of the fault is the same as in Fig. 4.4.

Again, the overall qualitative shape of the maps remains unchanged. As we can see in the wide pulse case, the use of the boxcar slip velocity function results in the lowest estimates of PGA when comparing with the results for the other two functions. This difference almost cannot be seen for the narrow pulse. The values nearly reach values for the instantaneous rise time. That is why we prefer the broad pulse. The effect of narrowing the slip pulse on the PGA maps is displayed in more detail (four values of L_0) in the figure 4.9 for Hisada's slip velocity function.

We can conclude that the instantaneous slip and the boxcar slip function are two unrealistic extremes among possible slip velocity functions. Moreover, the difference between the estimated PGA values for Hisada's and Brune's slip velocity functions is relatively small even for the wide slip pulses although their functional shape seems dissimilar. However, the unrealistic PGA values still remain. This lead us to consider a larger fault.

4.3 7.5×6 km fault model

Here we assume the fault of dimension 7.5×6 km and $K = 1$. Note that the mean slip was decreased in order to keep the scalar seismic moment unchanged. Hisada's and boxcar slip velocity functions and $L_0 = 0.20L$ are used to generate PGA maps in the figure 4.10 for two different realizations of slip distribution. Fig. 4.10 shows also the mean PGA map for 100 slip realizations. The map of variances is not displayed because it does not exhibit any systematic behaviour as in the previous case. The variances are about $25 - 35\%$.

In the figure 4.10 we can see similar quantitative and qualitative differences between the maps as in Fig. 4.8. The simulations with Hisada's slip velocity function give higher values of PGA than those corresponding to the boxcar function. Nevertheless, the shape of the maps, which is caused mainly by the directivity and the S wave radiation pattern, is very similar to each other. As it was expected, the simulated PGA values are lower than for the smaller 5×4 km fault.

The 7.5×6 km fault was found plausible by the PEXT simulation by *Zahradník* (submitted). However, constant slip is assumed in the PEXT method. Our heterogeneous slip results in higher PGA estimates (compare with the figure 4.3).

The K-parameter introduced in the slip distribution allows for modelling of smoother slip ($K < 1$). The slip distribution would be similar to the clipped constant slip for very small K (see figures A.1). The PGA maps for $K = 0.5$, $K = 1.0$ and $K = 2.0$ ($L_0 = 0.20L$) are displayed in the figure 4.11. As we can see, the higher K, the higher PGA. This confirms the theoretical result derived in the chapter 2.

The PGA values for $K = 0.5$ are still relatively high but it is obvious that we

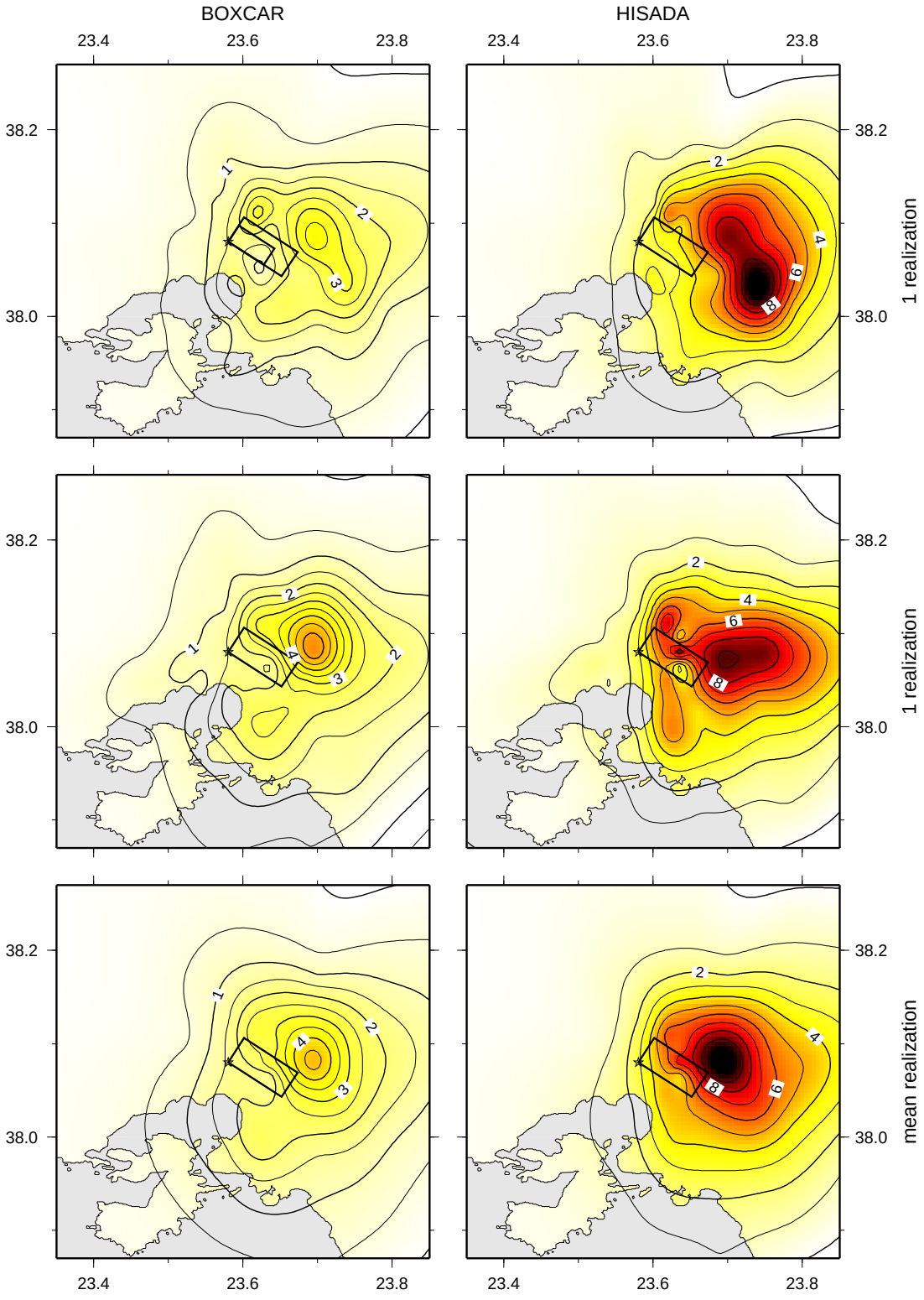

Figure 4.10: PGA maps in m/s^2 for 7.5×6 km fault model and two slip velocity functions. In the top and the middle part the figure shows results for two different realizations of the slip distribution. The mean result of 100 realizations is shown in the bottom. The rectangle in the middle of each map represents the projection of the fault to the earth's surface. For comparison, the 5×4 km fault studied before is displayed on the top left map. The star denotes the epicentre. $L_0 = 0.20L$.

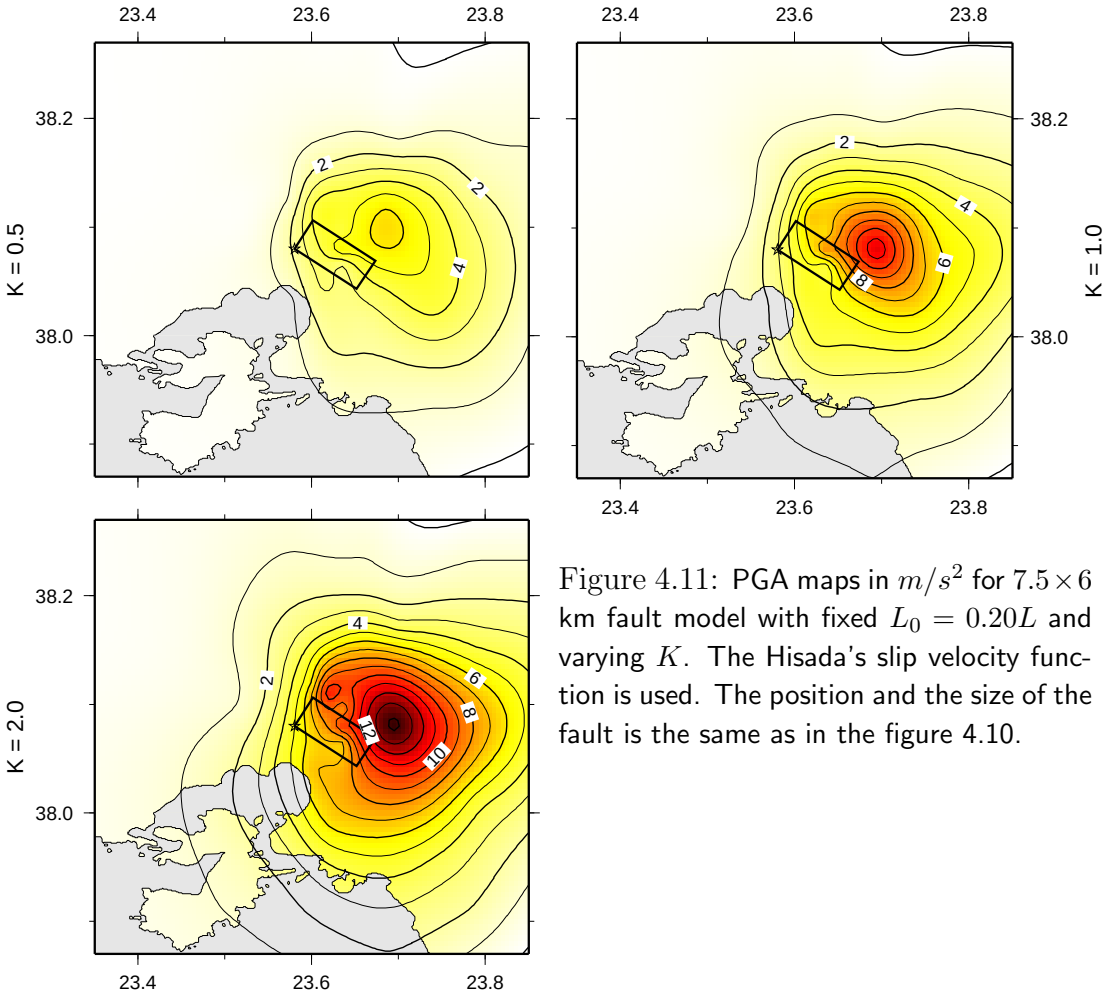

Figure 4.11: PGA maps in m/s^2 for 7.5×6 km fault model with fixed $L_0 = 0.20L$ and varying K. The Hisada's slip velocity function is used. The position and the size of the fault is the same as in the figure 4.10.

would reach PEXT simulation results by decreasing K. However, the slip would be smoothed.

Thus, one possibility is to extend the fault dimensions and keep K between 0.5 and 1.0 or to assume an asperity model of the rupture.

4.4 Asperity model

We choose two examples from a large set of possible asperity models: the "smaller" fault 10×8 km and the "larger" fault 15×12 km with an asperity 5×4 km and 7.5×6 km, respectively. The sizes as well as the positions of the asperities are chosen to correspond to the fault models discussed above. It means that the fault is extended in down-dip and along strike direction.

The width of the slip pulse corresponds to 20% of the asperity length L_a, thus, 10% of the fault entire length L, i.e. $L_0 = 0.20L_a = 0.10L$. To model the slip distribution with an asperity, we take advantage of our ability to combine the deterministic part of slip (asperity in our case) at low wave numbers and the stochastic k^{-2} distribution for the higher ones as it is described in the appendix A.2.

Another free parameter occurs in asperity models: contrast between the slip on the asperity versus the mean slip on the fault. We choose two slip contrast values: 2 and 3. The mean PGA maps for four cases (two dimensions of fault and two slip contrasts) are displayed in the figure 4.12. We can see that the simulated PGA values are realistic in these cases. The synthetic accelerograms and their amplitude spectra for various epicentral distances and azimuths are shown in the figure 4.13.

The two studies of empirical scaling laws for rupture properties mentioned in the chapter 1.3 give consistent parameters. The empirical relations of *Somerville et al.*, 1999 (summarised in the table 1.1 in this work) gives the area of the fault $A = 88$ km^2, which is only slightly larger than our case of 10×8 km. *Mai and Beroza*, 2000 (see formula (1.17) in this text) suggests a fault of dimension 12×9 km. The suggestion by *Somerville et al.*, 1999 that the asperity should cover about one quarter of the whole fault with twice higher slip than the mean slip is also consistent with our parameters. The average rise time $T_R = 0.4$ s given by *Somerville et al.*, 1999 is lower than our preferred maximum rise time (corresponding to the width of the slip pulse) of about 0.5s. On the other hand, the rise times for the slip wavelengths shorter than the slip pulse width are smaller in the k^{-2} rupture model, thus, the rise time given by the empirical relation should rather represent an "effective" value for this rupture model.

However, our parametric study of the rupture model cannot help us to decide whether the fault dimension was larger than 7.5×6 km without asperity or whether there were more asperities on relatively large fault and so on. Some other techniques inverting seismograms has to be used to obtain the slip model.

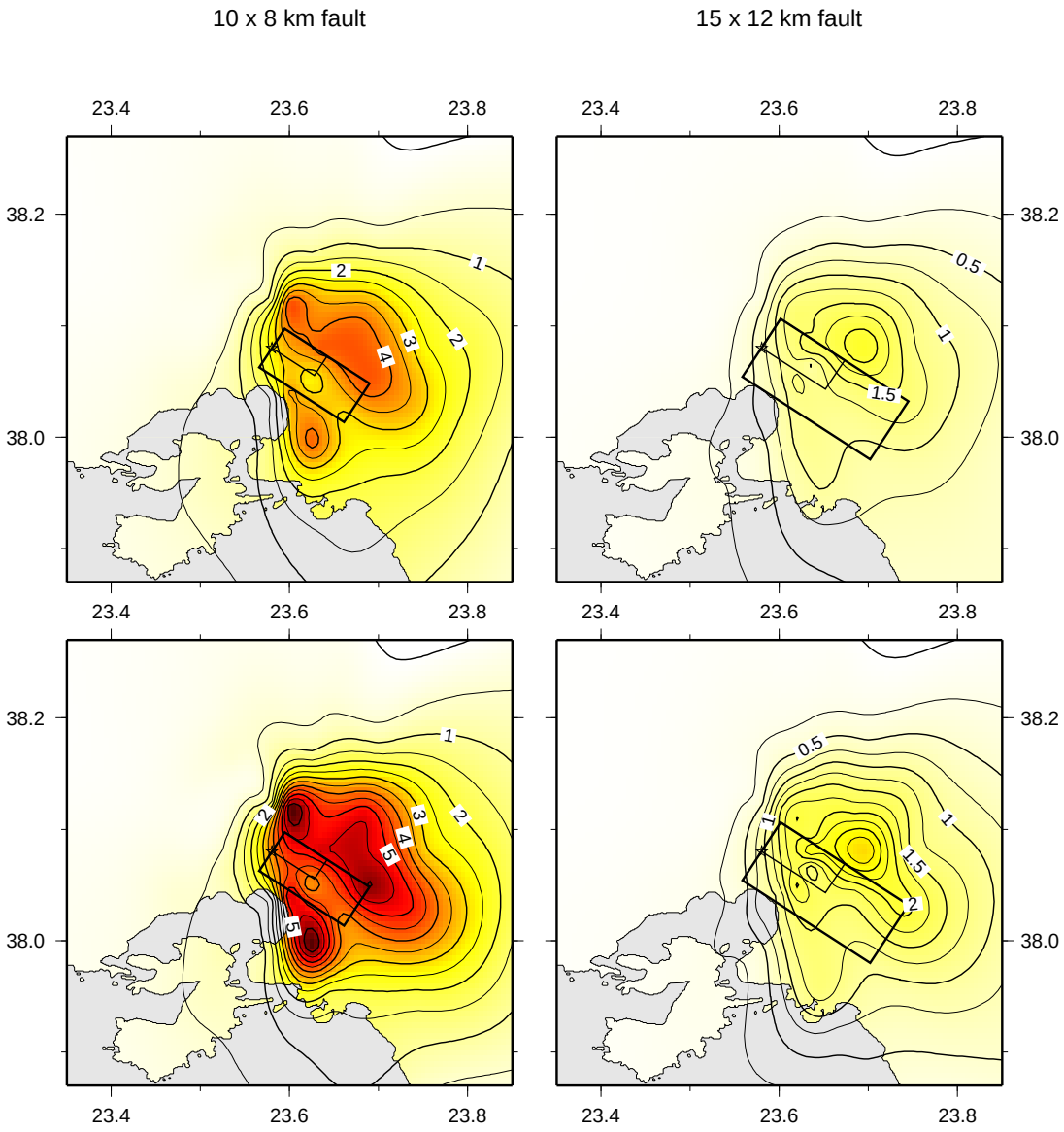

Figure 4.12: Mean PGA maps in m/s^2 over 100 realizations for various asperity models: two sizes of the entire fault (left, right) and two slip contrasts 2 (top) and 3 (bottom). The rectangles in the middle of each map represent the projections of the fault and the asperity to the earth's surface. The star denotes the epicentre. $L_0 = 0.20L_a$, $K = 1$, Hisada's slip velocity function.

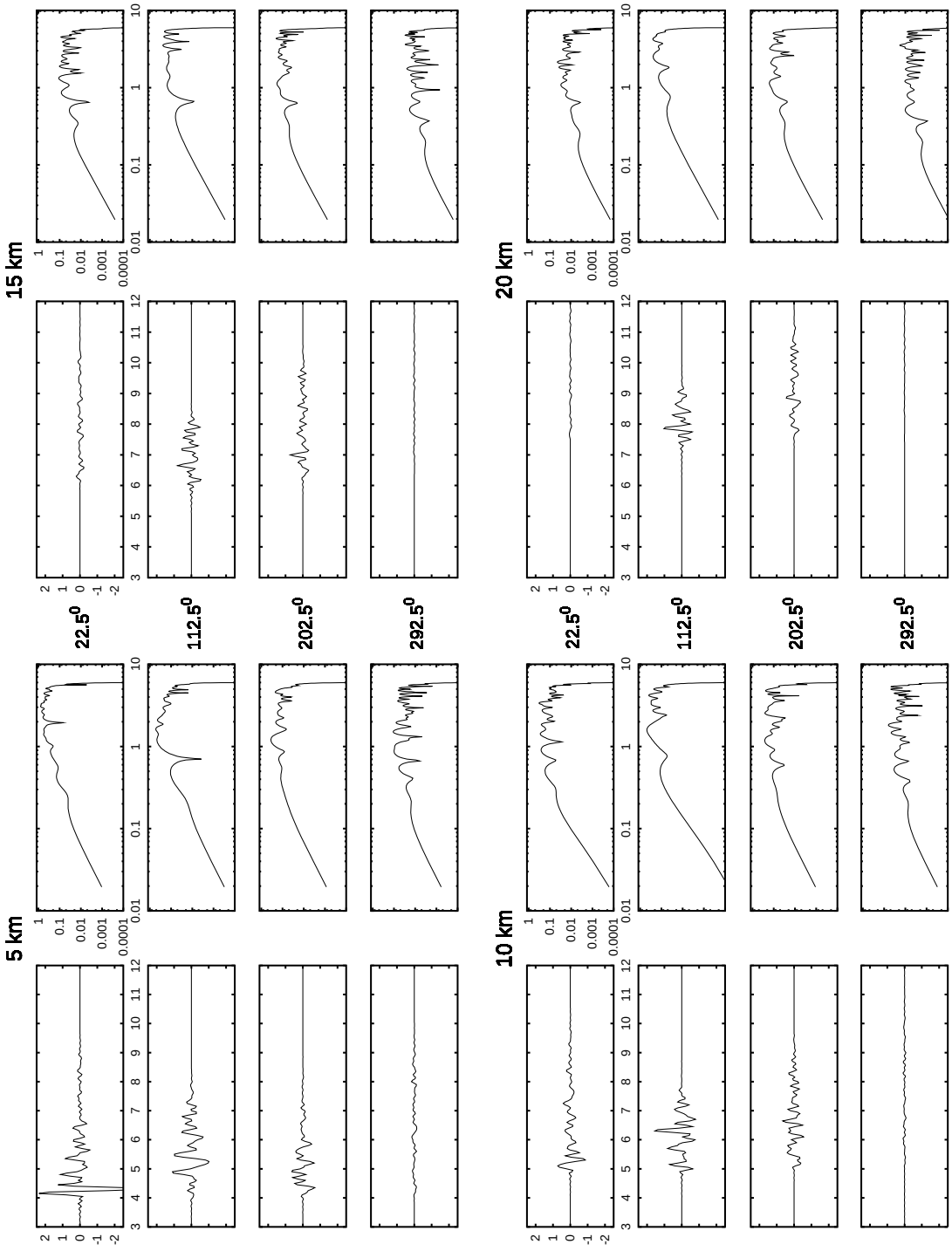

Figure 4.13: Each panel shows the synthetic accelerograms (in m/s^2) and their amplitude spectra at given epicentral distance for four azimuths of the stations (measured from north clockwise). The rupture model corresponds to a realization of the hybrid slip distribution for the case of 10×8 km fault with slip contrast 2. Note the effects of directivity: the amplitude and the width of the accelerogram, the height of the spectral plateau after the corner frequency and the shift of the corner frequency. The timescale is in seconds, the frequency scale in Hz.

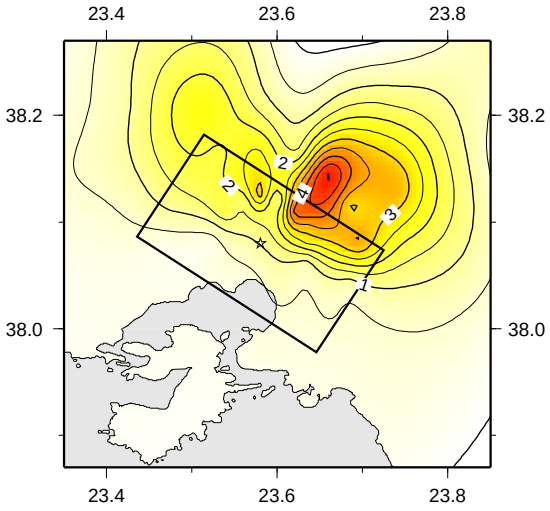

Figure 4.14: PGA map for slip model inverted by *Baumont et al.*, 2001. The slip pulse width is $L_0 = 1.9$km. The Hisada's slip velocity function is used. The rectangle in the middle of the map represents the projection of the fault of 22×22 km to the surface. The star denotes the epicentre.

4.5 Forward strong motion modelling for the slip obtained by inversion of seismograms

The EGF slip inversion was performed for the Athens earthquake by *Baumont et al.*, 2001 from regional data. The resultant slip distribution on 22×22 km fault and its hybrid k^{-2} modification can be found in the figure A.3. The strong motions are modelled with $L_0 = 1.9$km, which corresponds to the maximum rise time about 0.68s. The PGA map is displayed in the figure 4.14.

As we can see, the slip model moves the area of the highest PGA values slightly to the west (compare with our previous results). We cannot compare easily with the macroseismic data in the figure 4.2 since no direct intensity values are avaible from that area. Nevertheless, the overall pattern of the maximum PGA agrees with observation.

Note, the current state of the computing power of a standard PC allows for performing the slip inversion as well as the kinematic modelling for earthquakes with magnitudes comparable to the Athens earthquake nearly in real-time. If we believe that the slip inversion gives reasonable results, our procedure could help to assess the areas of the highest losses right after a damaging event. It can help to organize rescue operations.

Chapter 5

Discussion and conclusion

We have studied the k^{-2} kinematic rupture model proposed originally by *Bernard et al.*, 1996. It has been already successfully used for past as well as future earthquakes (e.g, *Berge-Thierry et al.*, 2001, *Zollo et al.*, 1997, *Emolo and Zollo*, 2001). All works emphasize the importance of considering the complexity of the source process for strong ground motions estimate in the near source region. Therefore, in this work we have generalized this model to provide a more flexible tool to simulate a larger variety of earthquakes. The four generalizations performed in this work are as follows:

1. The corner wave number in the k^{-2} stochastic slip distribution was generalized from $1/L$ to K/L (L being the fault length). The K-parameter consequently controls smoothness/roughness of the slip distribution. This parameter also affects the shape of the source spectrum: the corner frequency is proportional to K and the height of the spectral plateau to K^2. We suggest to study this parameter in more detail not only by analyzing the slip inversion results but also by studying the empirical attenuation relations.

2. An easy way to generate so-called hybrid slip (originally proposed by *Hisada*, 2001) was suggested. The hybrid slip consists of two parts. At low wave numbers the slip is deterministic, given by, e.g., empirical scaling laws (position of asperities subjected to variations and slip contrasts on them) or the slip inversion results. For the wavelenghts shorter than about the dimension of the deterministic part in the spatial slip spectrum, the slip is prescribed to have k^{-2} decay with a random phase. Such a hybrid model may represent more realistic slip distributions than the stochastic slip.

3. The unrealistic assumption of a boxcar slip velocity function (with wave number dependent rise time), discussed in *Bernard et al.*, 1996, was relaxed. It was found that arbitrary slip velocity function, which has its Fourier spectrum, possesing rise time proportional to the wavelength at high wave

numbers generates the desired omega-squared source spectrum. In other words, the spectral decay at frequencies higher than the corner frequency is given just by the decay of the slip distribution spectrum regardless on the type of the slip velocity function. This makes the ω-squared scaling law more robust. Moreover, it could also contribute to explanation of the empirical fact that ω-squared decay has been observed commonly. The assumption of wave number dependent rise time could be confirmed or refused by the dynamic rupture studies.

The study of the influence of various slip velocity functions on the ground acceleration has shown that the instantaneous slip and the boxcar function represent the limiting unrealistic cases. The instantaneous slip overestimates the accelerations while the boxcar slip velocity function underestimate them.

4. An easy way to incorporate the wave number dependent rise time in the representation theorem has been developed. The inverse spatial Fourier transform of the product of the slip distribution and the slip velocity function gives a unique slip function for each point on the fault. The ground motions are then obtained by the integration over the fault plane of Green's functions convolved with the slip functions from the previous step.

We have applied the k^{-2} rupture model to the 1999 Athens earthquake in order to compute the PGA maps in the vicinity of the fault. We fixed the earthquake parameters determined by previous studies: location of the epicentre, scalar seismic moment, focal mechanism, radial rupture velocity and the position of the nucleation point on the fault. The fact that the fault was buried about $5 - 7$ km under the surface allows us to assume that the direct S waves were responsible for the predominant phase in the strong ground motions.

The influence of remaining parameters of the k^{-2} rupture model (fault dimensions, slip pulse width, K-parameter and the shape of the slip velocity function) on PGA maps was studied. We have shown in a series of numerical experiments that the shape of the maps is given predominantly by the directivity and the radiation pattern. The fault dimensions together with the slip pulse width, K and the slip velocity functions change mainly the values of PGA. As regards the fault dimensions, they affects both the pattern of the PGA maps and the values of PGA. All these results of numerical experiments for 2D fault in a realistic 1D model can be understand in terms of the results derived for simple line fault in Fraunhoffer's approximation in homogeneous space (see Chap. 2). In the case of the asperity model, the asperity dimensions as well as the slip contrast also affect the PGA values considerably.

Our suggested set of k^{-2} rupture models suitable for the Athens earthquake (see Chap. 4.4) can explain the pattern of the macroseismic intensity map. We compared the suggested values of the kinematic parameters with the empirical

source scaling relations. The reasonable consistency gives us the hope that the source scaling laws by *Somerville et al.*, 1999, obtained basically from Californian earthquakes are applicable in the seismic hazard assessment in Attica. It means that we could be able to estimate strong ground motions of future event for given location and magnitude. Moreover, the hybrid slip model together with some fast slip inversion technique is applicable on fast estimations of highest damage areas after an event.

The remaining problems and outlines are as follows:

1. The most important problem of the high frequency kinematic modelling is the need of massive numerical computations. It is caused by the numerical evaluation of the representation theorem integral as well as the computation of a large set of Green's functions. In contrast, the rapidity of computations is the advantage of the composite and hybrid modelling.

2. The still remaining problem of k^{-2} rupture model is the assumption of constant rupture velocity. The influence of rupture time variations in the representation theorem on the generated wave field is not easy to handle even in the line fault approximation. However, it is clear that they are responsible for generation of high frequency waves. A first (numerical) attempt to incorporate the rupture time variations into kinematic modelling with constant rise time has been done by *Hisada*, 2000. Note that the influence of such variations on directivity is not yet resolved.

3. In our modelling, there is a strong assumption that the radiation pattern is the same at all frequencies. The wavefield at high frequencies is sensitive to small-scale variations of the rupture process, i.e., to spatial variations of rake or to non-planarities of the fault, etc. They have to be taken into account and further studied in order to find their consequences on the radiated wave field (particulary, on the directivity). The radiation pattern at high frequencies can be also smoothed out by scattering from small-scale heterogeneities in the Earth crust. These effects were not taken into account.

4. Besides PGA's, the response spectra should be studied for the Athens earthquake as one of the most used quantity in the engineering strong motion studies.

5. The attenuation (Q, κ) should be taken into account for better estimates of ground motions.

6. Note that the omega-squared source model has not yet been reliably confirmed. The critical task is to remove the propagation effects (e.g., attenuation, separation of direct P or S wave phases) from the recorded wave fields. In the k^{-2} rupture model, the decay exponent over ω is equal to the

exponent over k in the slip distribution. Moreover, the effect of directivity at high frequencies has not yet been reliably determined by empirical studies.

Appendix A

k^{-2} slip generation

In this part we explain the k^{-2} random dislocation distribution in detail.

Frankel, 1991, proposed that subevent distribution with the fractal dimension $D = 2$ and constant stress drop scaling (the mean slip is proportional to the fault length) produce the falloff f^{-2} of the high frequency radiation, provided the subevents fill in the whole fault area. *Herrero and Bernard*, 1994, introduce a kinematic self-similar random slip distribution with k^{-2} decay of Fourier amplitudes for high wave numbers and, consequently, k^{-1} decay for stress drop.

For 1D (linear) fault, the slip distribution function used in this work is described in the wave number domain by (2.7). Let us discuss the generalization to a 2D rectangular fault. The integration in the z-direction in the line fault approximation (see the derivation of (1.14)) can be interpreted as an integration along an isochrone parallel to the z-axes. If we deal with a general rectangular fault where the isochrones are more complex, it's reasonable to consider the spatial spectrum decay of the final slip as radially symmetric (*Bernard and Herrero*, 1994). This leads to the function

$$D(k_x, k_z) = \frac{\Delta\bar{u}LW}{\sqrt{1 + \left(\left(\frac{k_x L}{K}\right)^2 + \left(\frac{k_z W}{K}\right)^2\right)^2}} e^{i\Phi(k_x,k_z)}, \tag{A.1}$$

where $\Delta\bar{u}$ denotes the mean slip, Φ is the phase spectrum and L and W the length and the width of the fault, respectively. K is a dimensionless constant which influences the slip distribution and is discussed further in this appendix.

A.1 Random slip

In this case, the phase spectrum of (A.1) is considered random at any wave number, except for $k^2 \leq (1/L)^2 + (1/W)^2$ for which the phase is chosen in such a way to obtain the final slip concentrated in the centre of the rectangular fault. This also means that we have no other physical constraints on the dislocation

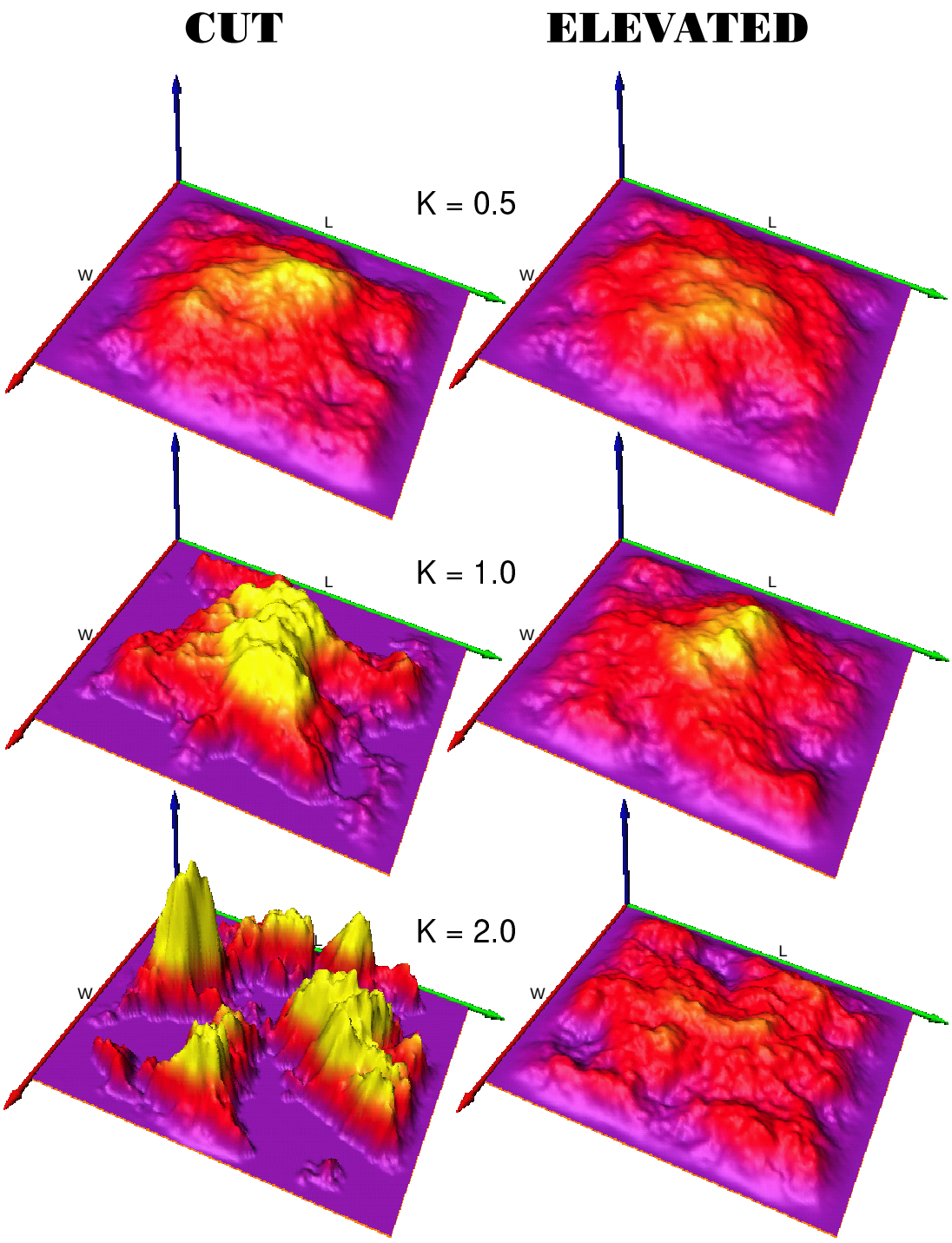

Figure A.1: Six different k^{-2} slip distribution for two different approaches to avoid negative slip as it is described in text. The parameter K changes the shape of final slip. The bigger K is the more the dislocation is "broken". Other consequences can be found in text. The mean slip is the same for all distributions.

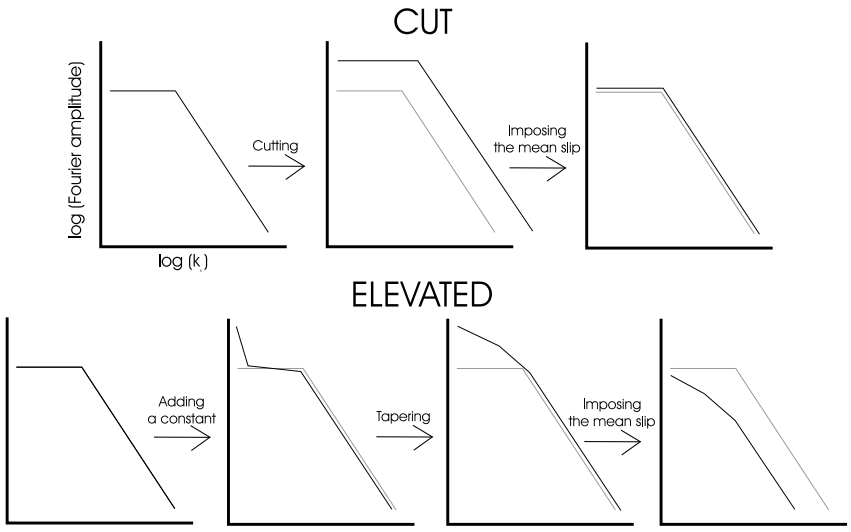

Figure A.2: A schematic picture of the influence of either cutting or elevating of the slip distributions on their spatial amplitude spectra. Only a cross-section $k_z = 0$ is shown for simplicity. The qray line represents the originally prescribed amplitude spectrum. Note how the elevation weakens the amplitudes at high wave numbers.

than the dimension of the fault and the mean slip. That's why we refer this as *random slip*. Examples of final slip for various K's (see (A.1))are shown in figure A.1. Here we give a brief description how to generate the final slip numerically:

- Random numbers are distributed in spatial domain on the discretised fault.
- The function is transformed to the wave number domain by performing 2D Fourier transform.
- The amplitudes of the spectrum are modified to correspond to (A.1). The phase for $k^2 \leq (1/L)^2 + (1/W)^2$ is changed to get the centre of the whole dislocation in the centre of the fault. The other phases (which are random) retain.
- The spectrum is transformed back into the spatial domain.
- To obtain a non-negative slip, the slip distribution has to be either elevated by adding a constant, or the negative numbers have to be cut. This step is discussed further in detail.
- The slip is tapered on the edges of the fault by a double cosine spatial window.

- Finally, the mean slip is imposed to the distribution to conserve seismic moment.

Let us discuss the problem of negative values of slip. According to *Bernard* (personal communication), in the figure A.2, it is illustrated how either cutting or elevating influences the high wave numbers.

Cutting. As the negative slip values are replaced by zeros the amplitude at zero wave number (integral over the fault) becomes larger. The amplitudes for other wave numbers become also higher due to the sharp edges caused by cutting. To impose the mean slip as the last step, the dislocation has to be multiplied by a constant less than 1. Consequently, the amplitude spectrum nearly returns to its original amplitudes for the whole wave number range.

Elevating. Adding a constant to the final slip changes the amplitude at zero wave number ($k_x = k_z = 0$) only. Tappering of the slip distribution expands the peak at zero wave number, i.e., it makes the amplitudes at long wavelengths dominant. After the last step of the generation procedure, the short wavelengths are even more weakened.

Note that for K smaller than 1 the small wave numbers are dominant to that extent that cutting or elevating is nearly not needed. However, for other K's, the procedure becomes important. Considering the elevation weakens short wavelengths, therefore we recommend cutting.

A.2 Hybrid slip

Let us note that considering a random slip is not very physical. Concentration of the seismic moment (slip) at the centre of the fault may be valid for small earthquakes, perhaps asperities but not for large ruptures. This is confirmed by various slip inversions yielding two or more asperities on the fault at random positions.

Another problem represents a broadband modelling for inverted slip models that are confined by limited resolution. Thus, the slip produced by slip inversion can be considered as a deterministic part of final slip at long wavelengths onto which a stochastic part is to be superimposed at wavelengths shorter than about the smallest dimension of the deterministic part.

It is obvious that random slip is one nonrealistic extreme case of possible slip models. The other nonrealistic extreme is the uniform slip. A real dislocation distribution lies somewhere between these two limiting cases.

These are the motivations to introduce so-called *hybrid slip* generator (*Hisada*, 2001). See two illustrative examples in the figure A.3. The procedure consists of four steps:

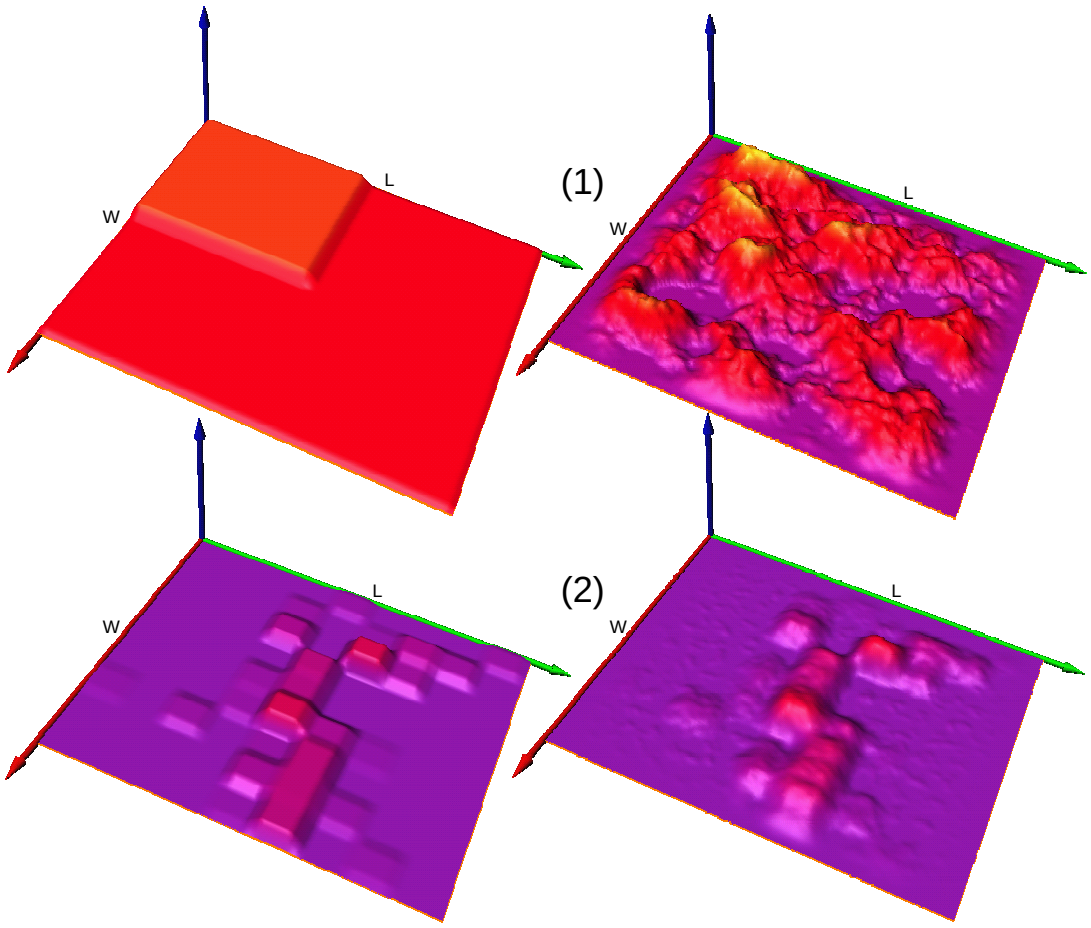

Figure A.3: Two examples of the hybrid slip: (1) a model with 1 asperity, (2) the hybrid slip created from the slip inversion result by *Baumont et al.*, 2001. The deterministic part of the slip distribution is displayed on the left side. The resulting hybrid slip (combination of the deterministic part and the k^{-2} amplitude spectrum (A.1) with random phase) is on the right side.

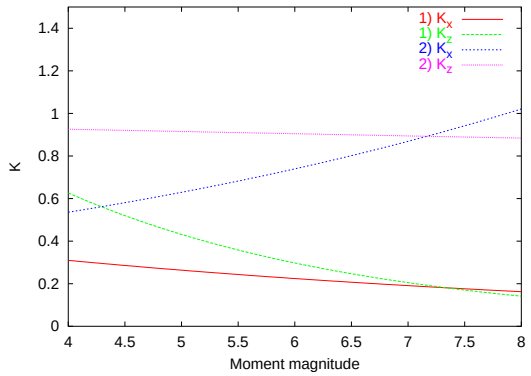

Figure A.4: The dependence of K on the moment magnitude M_w after two authors: 1) *Mai and Beroza*, 2001 and 2) *Somerville et al.*, 1999. K_x and K_z mean K in the strike and down dip direction, respectively. Let us note that both above mentioned papers prefere K rather less than 1 (corresponding to relatively smooth slip).

- Layout of the blocks of constant slip with the dimension of $\Delta L \times \Delta W$ representing the deterministic part of the slip (left side of the figure A.3).
- Smoothing by a sliding window.
- Transforming to the wave number domain
- Prescribing k^{-2} spectral decay by function (A.1) with random phase for $k > k_N$ where k_N is the Nyquist's wave number of the deterministic part ($k_N^2 = (1/\Delta L)^2 + (1/\Delta W)^2$). The deterministic shape will be preserved.

The deterministic part of the slip distribution (first step) can be obtained, for example, from slip inversions, from some empirical relations or from some known tectonic properties or constraints in the region.

The smoothing of the dislocation (second step) is necessary to avoid of the spectral holes caused by sharp edges of layout blocks[1]. *Hisada*, 2001, presents more complicated method of smoothing: first linear interpolation and then bicubic spline smoothing. However, we have found our easy method sufficient.

A.3 K-parameter

The scaling relation for the corner wave number in the slip distribution (A.1) has already appeared in papers dealing with the source scaling relations (*Somerville*, 1999, *Mai and Beroza*, 2000, *Main and Beroza*, 2001). They extract information about K-like-parameter (correlation length, i.e., L/K or W/K in our notation) from slip inversion results, i.e., from usually rough data with quite low confidence,

[1]The amplitude spectrum of a box corresponds to the function $\mathrm{sinc}(f)$. This oscillatory function reaches zero for some values of f. Such spectral holes are an artifact of the unphysical assumption that the deterministic part consists of blocks.

especially in the wave number domain (for tests of the slip inversion accuracy, see *Graves and Wald*, 2001, and *Wald and Graves*, 2001). Moreover, up to now there have been found (and examined) not more than about tens of slip models for magnitudes in the range about $5 < M_W < 8$
(see `http://www-socal.wr.usgs.gov/wald/slip_models.html` for available slip models of the western America earthquakes). Two empirical curves according to two authors showing the magnitude scaling of K are in the figure A.4.

We propose another way how to find a relation between, e.g., magnitude and the correlation length – to study horizontal peak ground acceleration (PGA) in the near source region and attenuation relations. Under attenuation relation we understand empirical relations between PGA and hypocentral distance for given magnitude, for an overview see *Abrahamson and Shedlock*, 1997. These relations usually more or less differ among particular authors or regions.

The theoretical Brune's omega-squared model is used to describe the source radiation as a function of earthquake magnitude. The geometrical spreading and the anelastic attenuation (i.e., propagation effects) are taken into account. Site effects are usually described by one variable, which differ from station to station.

Note that for our purpose the most reliable information lies in attenuation relations derived for a set of earthquakes of (nearly) the same magnitude within the same area. Consequently, the differences among them could be then linked to the K-parameter. Unfortunately, no such study exists.

The attenuation relations are studied usually for two ranges of magnitudes: from small to moderate sizes ($2 < M_W < 5$) and from moderate to large sizes ($4 < M_W < 7 - 8$). First, let us discuss the latter case. *Andrews*, 2001, studied the attenuation relation in California with a correction for a finite fault effect for small epicentral distances (that does not affect the information we want to extract). The author described the residuals from PGA regression, according to a prescribed fitting relation $f(M, R)$, by two random variables. Thus, his regression had the following form:

$$\ln PGA_{ij} = f(M_i, R_{ij}) + \eta_i + \epsilon_{ij}, \tag{A.2}$$

where R is the epicentral distance, subscripts i and j correspond to the event and record number, respectively, η_i is an interevent random variable with variance τ^2 and ϵ_{ij} is an intraevent random variable with variance σ^2. τ^2 can be linked to the variance of K because it corresponds to fluctuations of PGA's regardless of the moment and hypocentral distance. Its value was found by non-linear regression $\tau^2 = 0.032$. This suggests 20% variance for PGA. Consequently, for all considered magnitudes the K-parameter lies in the interval $0.9 - 1.1$ for the region of California since PGA is proportional to K^2 (see below). Such small variation of K can be linked to errors in the fitting procedure as well.

An open question still remains whether the range of K is the same for other regions with its tectonic regime and whether concluded fluctuation can be extrapolated to smaller magnitudes and other areas. Moreover, such slight fluctuation

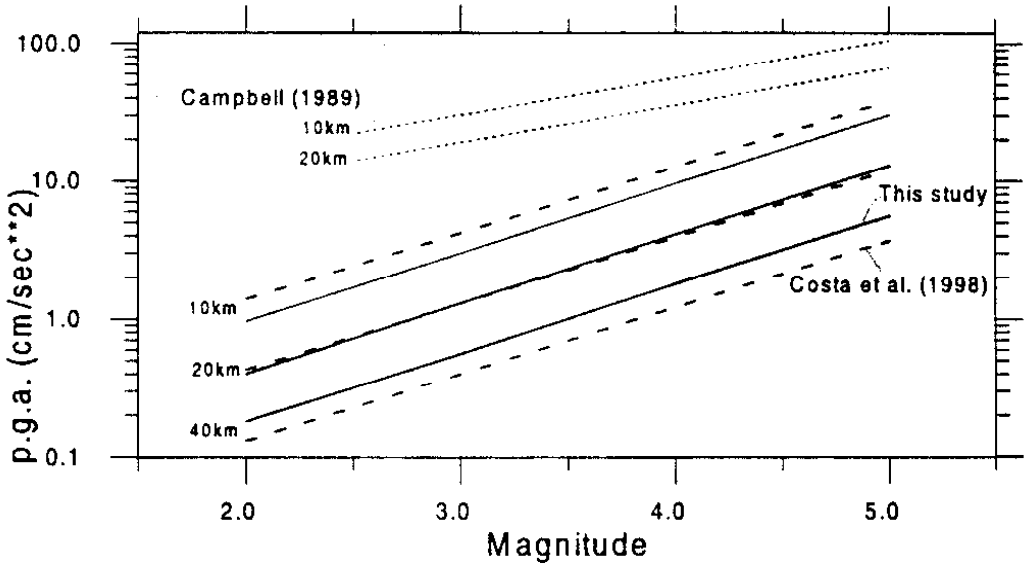

Figure A.5: A comparison of attenuation relations for weak-to-moderate earthquakes found for Greece (denoted as "this study"), Italy (Costa et al.) and California (Campbell). After *Theodulidis*, 1998.

can be still addressed to other, in the regression not accurately determined, quantities as well – they will be discussed further.

Let us discuss the attenuation relations for small-to-moderate events found for two nearby regions: Italy and Greece (*Theodulidis*, 1998). They can be found in the figure A.5. As it can be seen, they are very similar. On the other hand, Californian relations (*Campbell*, 1989, also in the figure A.5) predicts much higher (5-15 times) values of PGA. Could this suggest different correlation lengths of slip for these regions? Should it be that $K < 1$ or $K > 1$ for Greece (Italy)? To answer this, we have to recall that (see section 2.2) the height of acceleration spectral plateau and the corner frequency are proportional to K^2 and K, respectively. If the steep spectral falloff after f_{max} was not present, the PGA (related to the root mean square acceleration a_{rms}, which is equal to square root of the power spectrum integral due to the Rayleigh's theorem) would be still higher for higher K, proportional to approximately K^2. Otherwise, if the falloff after f_{max} is present, then as the corner frequency approaches f_{max}, the PGA value gets smaller (for rising K). This suggests that for Greece K is probably less or slightly more than 1.

These were only motivations for studying the dependence of the corner wave number on the magnitude not only from slip inversions but also from attenuation relations. We recommend to study this topic deeply because there are (as in slip inversions) lots of biases that have to be sensitively considered. Let us discuss

them here in a little more detail.

- The correction for the radiation pattern is not appropriately (if ever) discussed in any of the referred papers. We have to believe that this effect was taken into account but still we have to keep in mind that this could be questinable. The determination of the focal mechanism for small magnitude earthquakes is quite inaccurate. On the other hand, in case of large earthquakes, the effect of the radiation pattern could be quite smoothed due to the finiteness of the fault.

- It should be investigated how the K-parameter affects, for example, the estimation of the fault dimension or the stress drop.

- In referred papers, prescribed source model contains only epicentral (hypocentral) distance, not the hypocentral depth. It is not clear whether the depth of the source was excluded for simplification or it does not affect the results significantly.

- The value of f_{max} is very important in PGA estimations. It is demonstrated by *Campbell*, 1989. The attenuation relation were found for California where f_{max} does not exceed approximately 25Hz. The author has to restrict the range of interest to frequencies lower than 25Hz to obtain consistent predictions for (i.e., extrapolate the Californian to) Northeastern America earthquakes where f_{max} can be more than 50Hz.

- The differences in regional magnitude scales can produce significant systematic errors and cause problems in comparisons of attenuation relations among various areas.

- Other quantities uncertain in determination and biasing the attenuation relations are, e.g., unelastic attenuation (*Rovelli et al.*, 1991) and site effects (caused by, for example, lateral inhomogeneities, 3D site effects, etc.).

Despite of these problems, the correlation length (and K) should be investigated, since its most important property is that it affects values of strong ground motions regardless of magnitude or propagation effects.

References

Abrahamson, N. A., Bolt, B. A. (1987). Arrays Analysis and Synthesis Mapping of Strong Seismic Motion, in *Seismic Strong Motion Synthetics*, B. A. Bolt (Editor), Academic Press, Orlando, Florida, 205–265.

Abrahamson, N. A., Shedlock, K. (1997). Overview. *Seis. Res. Letters* **68**, 9–23.

Aki, K., Richards, P.G. (1980). Quantitative Seismology: Theory and Methods. *W.H. Freeman, San Francisco.*

Andrews, D. (2001). A Suggestion for Fitting Ground-motion Attenuation near an Extended Earthquake Source. *Seis. Res. Letters* **72**, 454–461.

Baumont, D., Courboulex, F., Scotti, O., Melis, N. S., Stavrakakis, G. Slip Distribution of the $M_w = 5.9$, 1999 Athens Earthquake Inverted from Regional Seismological Data, *submitted to Geoph. Res. Letters.*

Beresnev, I. A. and Atkinson, G. M. (1997). Modeling Finite-Fault Radiation from the w^n Spectrum, *Bull. Seism. Soc. Am.* **87**, 67–84.

Berge-Thierry, C., Bernard, P., Herrero, A. (2001). Simulating Strong Ground Motion with the "k^{-2}" Kinematic Source Model: An Application to the Seismic Hazard in the Erzincan basin, Turkey, *Journal of Seismology* **5**, 85–100.

Bernard, P. and Herrero, A. (1994). Slip Heterogeneity, Body-Wave Spectra, and Directivity of Earthquake Ruptures, *Annali di Geofisica*, Vol. **XXXVII**, 1679–1690.

Bernard, P., Herrero, A. and Berge, C. (1996). Modeling Directivity of Heterogeneous Earthquake Ruptures, *Bull. Seism. Soc. Am.* **86**, 1149–1160.

Brokešová, J. (1993). High-frequency ground motions due to extended seismic sources in complex structures. *PhD. Thesis,* Charles University, Prague.

Campbell, K. W. (1989). The Dependence of Peak Horizontal Acceleration on Magnitude, Distance and Site Effects for Small-magnitude Earthquakes in California and Eastern North America. *Bull. Seism. Soc. Am.* **79**, 1311–1341.

Cotton, F., Campillo, M. (1995). Frequency Domain Inversion of Strong Motion: Application to the 1992 Landers Earthquake, *Journal of Geophysical Research*, Vol. **100**, 3961–3975.

Červený, V. (1985). Ray Synthetic Seismograms for Complex Two-Dimensional and Three-Dimensional Structures, *Journal of Geophysics* **58**, 2–26.

Červený, V., Molotkov, I. A., Pšenčík, I. (1977). Ray Method in Seismology, *Charles University, Prague.*

Emolo, A., Zollo, A. (2001). Accelerometric Radiation Simulation for the September 26, 1997 Umbria-Marche (Central Italy) Main Shocks. *Annali di Geofisica* **44**, 605–617.

Farra, V., Bernard, P., Madariaga, R. (1986). Fast Near Source Evaluation of Strong Ground Motion for Complex Source Models. *Maurice Ewing Volume 6 of Geophysical Monograph 37*, American Geophysical Union, pp. 121–130.

Frankel, A., Clayton, R. W. (1986). Finite Difference Simulations of Seismic Scattering: Implications for the Propagation of Short-period Seismic Waves in the Crust and Models of Crustal Heterogeneity. *Journal of Geophysical Research*, Vol. **91**, 6465–6489.

Frankel, A. (1991). High-Frequency Spectral Falloff of Earthquakes, Fractal Dimension of Complex Rupture, *b* Value, and the Scaling of Strength on Faults, *Journal of Geophysics* **96**, 6291–6302.

Gasperini, P. (2001). The Attenuation of Seismic Intensity in Italy: A Bilinear Shape Indicates the Dominance of Deep Phases at Epicentral Distances Longer than 45 km. *Bull. Seism. Soc. Am.* **91**, 1–15.

Graves, R., Wald, D. (2001). Resolution Analysis of Finite Fault Source Inversion Using One- and Three-dimensional Green's Functions, 1. Strong Motions. *Journal of Geophysical Research*, Vol. **106**, 8745–8766.

Hanks, T. C. (1982). fmax. *Bull. Seism. Soc. Am.* **72**, 1867–1879.

Hartzell, S., Harmsen, S., Frankel, A., Larsen, S. (1999). Calculation of Broadband Time Histories of Ground Motion: Comparison of Methods and Validation using Strong-Ground Motion from the 1994 Northridge Earthquake, *Bull. Seism. Soc. Am.* **89**, 1484–1504.

Heaton, T. H. (1990). Evidence for and Implications of Self-healing Pulses of Slip in Earthquake Rupture. *Phys. Earth Planet. Interiors* **64**, 1–20.

Herrero, A., Bernard, P. (1994). A Kinematic Self-Similar Rupture Process for Earthquakes, *Bull. Seism. Soc. Am.* **84**, 1216–1228.

Hisada, Y. (2000). A Theoretical Omega-Square Model Considering the Spatial Variation in Slip and Rupture Velocity, *Bull. Seism. Soc. Am.* **90**, 387–400.

Hisada, Y. (2001). A Theoretical Omega-Square Model Considering the Spatial Variation in Slip and Rupture Velocity. Part 2: Case for a Two-Dimensional Source Model, *Bull. Seism. Soc. Am.* **91**, 651–666.

Irikura, K., Kamae, K. (1994). Estimation of Strong Ground Motion in Broad-frequency Band Based on a Seismic Source Scaling Model an Empirical Green's Function Technique, *Annali di Geofisica,* VOL **XXXVII**, 1721–1743.

King, G. C. P., Stein, R. S., Lin J. (1994). Static Stress Changes and the Triggering of Earthquakes. *Bull. Seism. Soc. Am.* **84**, 935–953.

Kontoes, C., Briole, P., Sachpazi, M., Veis, G., Elias, P., Kotsis, I., Sykioti, O., Remy, D. Displacement Field Mapping and Fault Modeling of the $M_w = 5.9$, September 7, 1999 Athens Earthquake Based on ERS-2 Satellite Radar Interferometry, *submitted to Geoph. Res. Letters.*

Mai, M. and Beroza, C. (2000). Source Scaling Properties from Finite-Fault Rupture Models, *Bull. Seism. Soc. Am.* **90**, 604–615.

Mai, P.M., and G.C. Beroza (2001). A Spatial Random-Field Model to Characterize Complexity in Earthquake Slip. *J. Geophys. Res.*, in review.

Novotný, O., Zahradník, J., Tselentis, G. A. (2001). Northwestern Turkey Earthquakes and the Crustal Structure Inferred from Surface Waves Observed in Western Greece. *Bull. Seism. Soc. Am.* **91**, 875–879.

V. Plicka and J. Zahradník (2001). Inversion of Rupture Nucleation from Regional Records by EGF Method for Unequal Focal Mechanisms of the Mainshock and Aftershock: The Athens 1999 Earthquake, *submitted to Tectonophysics*.

Rovelli, A., Cocco, M., Console, R., Alessandrini, B., Salvatore, M. (1991). Ground Motion Waveforms and Source Spectral Scaling from Close-distance Accelerograms in a Compressional Regime Area (Friuli, Northeastern Italy). *Bull. Seism. Soc. Am.* **81**, 57–80.

Somerville, P., Irikura, K., Graves, R., Sawada, S., Wald, D., Abrahamson, N., Kagawa, Y. I. T., Smith, N., Kowada, A. (1999). Characterizing Crustal Earthquake Slip Models for the Prediction of Strong Ground Motion. *Seis. Res. Lett.* **70**, 59–80.

Spudich, P. and Frazer, L. N. (1984). Use of Ray Theory to Calculate High-Frequency Radiation from Earthquake Sources Having Spatially Variable Rupture Velocity and Stress Drop. *Bull. Seism. Soc. Am.* **74**, 2061–2082.

Spudich, P. and Archuleta, R. J. (1987). Techniques for Earthquake Ground-Motion Calculation with Applications to Source Parametrization of Finite Faults, in *Seismic Strong Motion Synthetics*, B. A. Bolt (Editor), Academic Press, Orlando, Florida, 205–265.

Theodulidis, N. P. (1998). Peak Ground Acceleration Attenuation of Small Earthquakes: Analysis of Euroseistest, Greece, data in *The Effects of Surface Geology on Seismic Motion*, Irikura, Kudo, Okada, Sasatani (Editors), Balkema, Rotterdam, 1171–1176.

Tselentis, G. A., Zahradník, J. (2000a). Aftershock Monitoring of the Athens Earthquake of 7 September 1999. *Seis. Res. Lett.* **71**, 330–340.

Tselentis, G. A., Zahradník, J. (2000b). The Athens Earthquake of 7 September 1999. *Bull. Seism. Soc. Am.* **90**, 1143–1160.

Wald, D. and Heaton, T. (1994). Spatial and Temporal Distribution of Slip for the 1992 Landers, California, Earthquake. *Bull. Seism. Soc. Am.* **84**, 668–691.

Wald, D., Graves, R. (2001). Resolution Analysis of Finite Fault Source Inversion

Using One- and Three-dimensional Green's Functions, 2. Combining Seismic and Geodetic Data. *Journal of Geophysical Research*, Vol. **106**, 8767–8788.

Wessel, P., Smith, W.H.F. (1991). Free Software Helps Map and Display Data. *EOS Trans. AGU* **72**, 441, 445–446.

Willmore, P. L. (1977). World Data Center A for Solid Earth Geophysics. Report SE-20: Manual of Seismological Observatory Practice. *Boulder, Colorado.*

Zahradník, J. Focal Mechanism of the Athens 1999 Earthquake by ASPO Method, *submitted to Tectonophysics*.

Zahradník, J., Tselentis, G. A. Modelling of Strong Motion Accelerograms by PEXT Method, Application to the Athens 1999 Earthquake, *submitted*.

Zollo, A., Bobbio, A., Emolo, A., Herrero, A., De Natale, G. (1997). Modeling of Ground Acceleration in the Near Source Range: the Case of 1976, Friuli Earthquake (M=6.5), Northern Italy. *Journal of Seismology* **1**, 305–319.